Article

Isolated theta waves originating from the midline thalamus trigger memory reactivation during NREM sleep in mice

Qin Xiao[1,9], Minmin Lu[1,9], Xiaolong Zhang[1], Jiangheng Guan[2], Xin Li[1], Ruyi Wen[1], Na Wang[1], Ling Qian[1], Yixiang Liao[1], Zehui Zhang[3], Xiang Liao[4], Chenggang Jiang[5], Faguo Yue[6], Shuancheng Ren[1], Jianxia Xia[1], Jun Hu[7], Fenlan Luo[1]✉, Zhian Hu[1,8]✉ & Chao He[1]✉

During non-rapid eye movement (NREM) sleep, neural ensembles in the entorhinal-hippocampal circuit responsible for encoding recent memories undergo reactivation to facilitate the process of memory consolidation. This reactivation is widely acknowledged as pivotal for the formation of stable memory and its impairment is closely associated with memory dysfunction. To date, the neural mechanisms driving the reactivation of neural ensembles during NREM sleep remain poorly understood. Here, we show that the neural ensembles in the medial entorhinal cortex (MEC) that encode spatial experiences exhibit reactivation during NREM sleep. Notably, this reactivation consistently coincides with isolated theta waves. In addition, we found that the nucleus reuniens (RE) in the midline thalamus exhibits typical theta waves during NREM sleep, which are highly synchronized with those occurring in the MEC in male mice. Closed-loop optogenetic inhibition of the RE-MEC pathway specifically suppressed these isolated theta waves, resulting in impaired reactivation and compromised memory consolidation following a spatial memory task in male mice. The findings suggest that theta waves originating from the ventral midline thalamus play a role in initiating memory reactivation and consolidation during sleep.

Neural ensemble interactions in the medial entorhinal cortex (MEC)-hippocampal circuit support learning and memory[1–3]. During wakefulness, specific neural ensembles are activated, exhibiting theta and gamma oscillations, to achieve encoding and retrieval of memories with the help of wakefulness-promoting systems[4–9]. These neural ensembles are reactivated during non-rapid eye movement (NREM) sleep, coordinated by network oscillatory events known as sharp-wave ripples (SWRs) and cortical spindles. Reactivation during NREM sleep is considered as one of the cellular hallmarks of memory and plays a necessary role in the formation of stable memory[10–12]. The impairment of reactivation is closely linked to memory dysfunction and may contribute to cognitive decline in those with Alzheimer's disease[13–15].

[1]Department of Physiology, Third Military Medical University, Chongqing, China. [2]Department of Neurosurgery, General Hospital of Chinese PLA Central Theater Command, Wuhan, China. [3]Department of Physiology, College of Basic Medical Sciences of Jilin University, Changchun, China. [4]Center for Neurointelligence, School of Medicine, Chongqing University, Chongqing, China. [5]Department of Sleep and Psychology, Chongqing Health Center for Women and Children, Chongqing, China. [6]Sleep and Psychology Center, Bishan Hospital of Chongqing Medical University, Chongqing, China. [7]Department of Neurology, Southwest Hospital, Third Military Medical University, Chongqing, China. [8]Chongqing Institute for Brain and Intelligence, Guangyang Bay Laboratory, Chongqing, China. [9]These authors contributed equally: Qin Xiao, Minmin Lu. ✉e-mail: fenlanluo@163.com; zhianhu@aliyun.com; hechaochongqing@163.com

However, to date, the neural mechanisms responsible for the generation of memory-related neural ensemble reactivation during sleep still remain elusive. The elucidation of these mechanisms has become a fundamental concern in understanding the role of sleep in the memory consolidation.

The reactivation of neural ensembles and the associated high-frequency network oscillations in the MEC generally necessitates excitatory subcortical inputs, as it cannot be solely achieved by the MEC alone[16–19]. The MEC-hippocampal circuit receives various external inputs, including wakefulness-promoting neurons, such as cholinergic neurons in the basal forebrain[6–8,20], histaminergic and hypocretinergic neurons in the hypothalamus[4,5], as well as inputs from the midline thalamus[21,22]. In fact, these cholinergic and monoaminergic neurons exhibit peak activity during wakefulness, driving the high-frequency oscillations like theta and gamma oscillations required for memory encoding and recall during wakefulness. However, following the transition from wakefulness to NREM sleep, their firing activity significantly diminished, suggesting a limited role in driving reactivation and high-frequency oscillatory events during NREM sleep[4,7,8,20]. In contrast, the midline thalamic neurons display distinct characteristics compared to these wakefulness-promoting neurons and continue to exhibit burst firing during NREM sleep[21,23]. Additionally, many studies have reported that midline thalamus is implicated in the memory performance[21,24–27]. Therefore, we hypothesize that the midline thalamus may play a crucial role in driving reactivation of neural ensembles associated with memory consolidation during NREM sleep.

We focused specifically on the MEC associated with spatial memory, and demonstrated that isolated theta waves, nested within the delta waves, are in concert with the reactivation of MEC cells during NREM sleep after spatial memory training. In addition to the previously reported neocortical slow oscillations (SO)-coupled spindle waves and hippocampal SWRs[10,28], our present results unveil that isolated theta waves serve as the sign of memory replay. Concurrently, we show that the nucleus reuniens (RE) in the midline thalamus exhibits isolated theta waves which propagate to the MEC and trigger memory reactivation in the MEC. Taken together, this study identifies a network oscillation pattern associated with memory consolidation during sleep and reveals that the midline thalamus has a unique role in this process.

Results

The reactivation of cell ensembles manifests as isolated theta waves during NREM sleep

To explore whether the MEC replays waking experience, we developed a six-arm maze task to assess the spatial memory, in which animals had to learn to select the rewarded arm. After six trials per day for consecutive three days of training during light phase (12:00 P.M.–18:00 P.M.), the animal gradually gained stable spatial memory, manifested as reaching the rewarded arm with a shorter path (Fig. 1A–D). According to previous reports on the effect of different sleep duration on memory consolidation, spatial memory consolidation could be effectively achieved within 1 h after training with 15–30 min NREM sleep[29–31]. Therefore, we recorded spikes and local field potentials (LFP) from the superficial layers of the MEC, in conjunction with electroencephalography (EEG) and electromyography (EMG) recordings, immediately after spatial memory training during the light phase. During this phase, animals spent about 50% of the time in the NREM sleep on average; however, they spent very little time in rapid eye movement (REM) sleep (Supplementary Fig. 1). Therefore, we focused only on NREM sleep in the subsequent analyses.

A total of 117 and 129 neurons were recorded on day 1 and day 2, with putative interneurons comprising only 18% and 13%, respectively. We used principal components (PC) analysis to extract the firing patterns of all the neurons during the learning phase. High-rank PC, associated with larger eigenvalues that exceeded the signal threshold defined as the theoretical upper bound for eigenvalues in the case of

random spike trains, were referred to as signal PC. After detecting the signal PC, we calculated the reactivation strength during post-training sleep. Of note, high reactivation strength reflects that the firing pattern during NREM sleep is a closer match to learning-related firing pattern[32,33]. Figure 1E shows an example of a firing pattern of MEC neurons with a signal PC and corresponding reactivation strength during post-training NREM sleep and wakefulness. Of note, high reactivation strength was detected during NREM sleep rather than wakefulness. On average, a significant increase in the strength of reactivation events was observed during the NREM sleep period relative to post-training wakefulness (Fig. 1F and Supplementary Fig. 2A–D). There was no significant difference in the average reactivation strength during NREM sleep between the first and second day of training (because the mice had already acquired stable spatial memory by the third day of testing, we focused on memory consolidation only after the first and second days of training) (Supplementary Fig. 2E).

To further analyze the spatial memory features reflected by the detected signal PC that were reactivated during NREM sleep, the normalized Z-scores in different positions of the maze were introduced to quantify the activation strength of the signal PC in each corresponding trial. A higher z-score at specific location in the maze indicates that the signal PC prefers to appear at that location. The preferential position of signal PC covered the different arms of the maze, including the start arm (cluster 1), turning points (cluster 2), non-reward arms (cluster 3) and reward arm (cluster 4) (Supplementary Fig. 2F–H). The cluster 1 and 2 accounted for the proportion of 28% and 49%, while the cluster 3 and 4 were 10% and 13%, respectively (Supplementary Fig. 2I). These findings indicated that the firing patterns of MEC cells were indeed correlated with different parts of the six-arm maze during training phase and reactivated during post-training NREM sleep.

Many studies reported that neural reactivations during NREM sleep are coordinated by prominent network oscillations, e.g. SO-coupled spindle waves in the neocortical regions and SWRs in the hippocampus[11,34,35]. Yet, the signature of network oscillatory dynamics reflecting the replay of MEC cells remains unclear. After entering NREM sleep, the delta oscillations (0.5–4 Hz) and low-frequency theta (4–6 Hz) increased significantly, but the high-frequency theta (6–12 Hz) decreased significantly (Supplementary Fig. 3). After analyzing the power spectrum of the LFP by wavelet transform, discreted theta events in the MEC recordings were evident during NREM sleep (Fig. 1G). These theta events during NREM sleep lasted about 300 ms (The term "isolated theta waves" is used to describe these theta events due to their short duration) (Fig. 1H). During isolated theta wave phase, the percentage of theta band power is significantly higher than that of non-isolated theta wave phase (Fig. 1I). Notably, these isolated theta waves occurred phase-locked to the depolarizing up-state of the delta waves, since the modulation index (MI) was higher compared to that of the shuffled data (Fig. 1J–M).

Additionally, examining data from entire post epoch sessions revealed that reactivation peaks occurred concomitantly with isolated theta waves. Significant reactivation events (R_T), defined as their reactivation values exceeding the threshold (mean plus 3 standard deviation of the reactivation values from entire post NREM sleep epoch sessions), mainly occurred in the up-state of the delta waves, where prominent isolated theta waves were nested (Fig. 1N, O). Power spectrum analysis further showed that significant reactivation events were indeed accompanied by stronger theta waves compared to the baseline (inset in Fig. 1P). Altogether, these results suggested that delta waves-nested isolated theta waves are in concert with the replay of MEC cells.

RE exhibits typical isolated theta waves that can propagate to the MEC through excitatory monosynaptic transmissions

The delta waves have been considered to primarily generate within cortical networks, where it can occur in the absence of thalamocortical
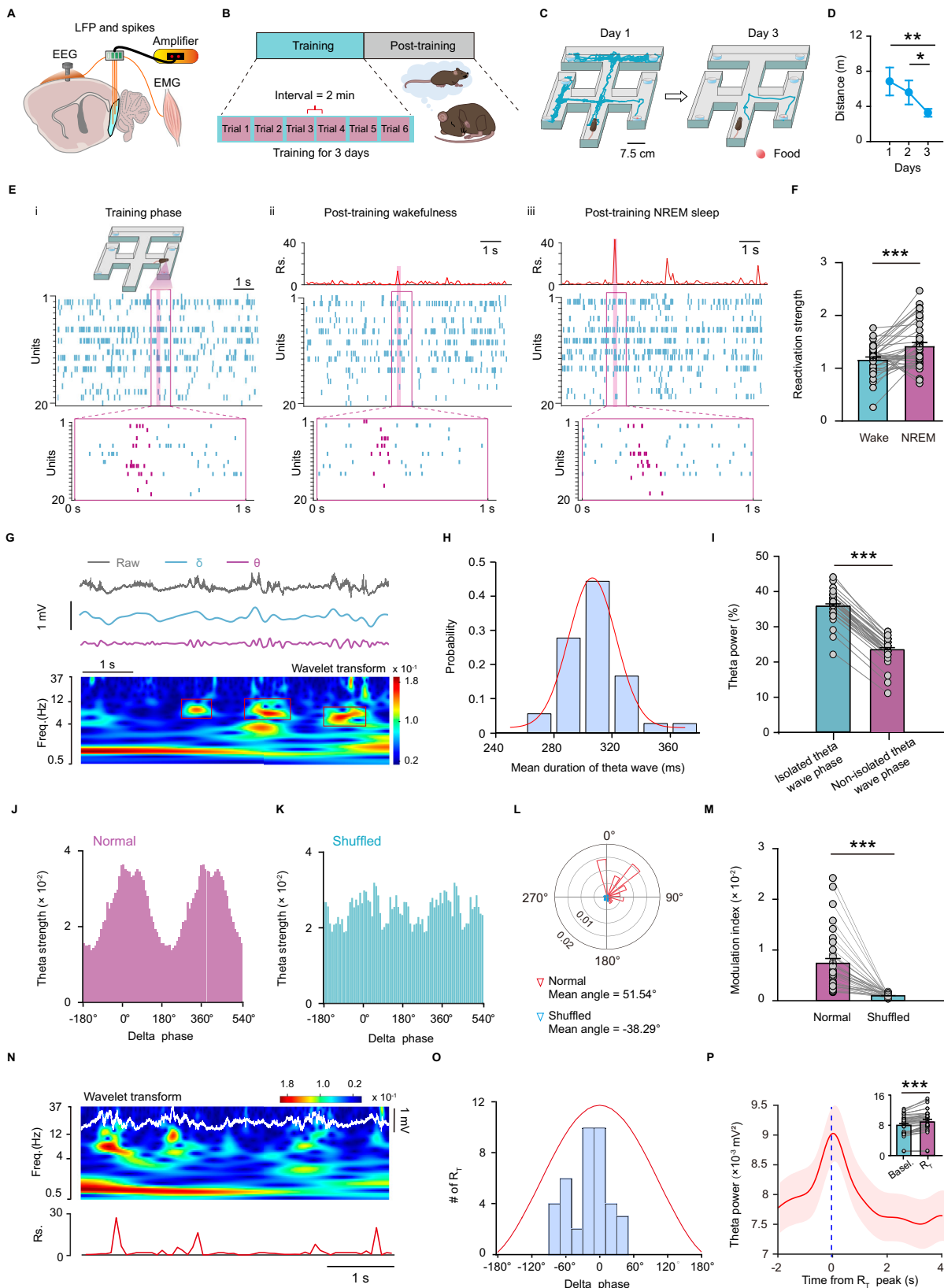
input, and are closely associated with the homeostatic functions of NREM sleep[17–19]. Nonetheless, the occurrence of high-frequency network oscillations in the neocortex and hippocampus, such as the spindles and theta waves, often requires external excitatory inputs[4,20]. Then, we want to determine the excitatory inputs that drive isolated theta waves in the MEC. Using a monosynaptic retrograde tracing technique based on glycoprotein (G)-deleted rabies virus, we screened the upstream targets of the MEC, which include RE in the midline thalamus, medial septum/diagonal band, hippocampus and piriform cortex (Supplementary Fig. 4A–D). Among these brain areas, the RE in the midline thalamus has attracted our attention, because the glutamatergic neurons in the RE of the midline thalamic nuclei can generate

Fig. 1 | Reactivation of MEC cells manifests isolated theta waves during NREM sleep. A, B Schematic diagram depicting LFP and EEG-EMG recording (**A**), and spatial memory task (**B**). **C** Representative trajectories on first and third day training sessions. **D** Distance that animals traveled in the maze (one-way repeated measures ANOVA followed by post hoc Fisher LSD Method, $n = 6$ mice, $F_{2,5} = 7.069$, $P = 0.012$; day 1 vs. day 3, $P = 0.004$; day 1 vs. day 2, $P = 0.224$; day 2 vs. day 3, $P = 0.037$). **E** MEC neuronal activity recorded during training phase (i), post-training wakefulness (ii) and post-training NREM sleep (iii) with a magnified view of a firing pattern (marked by magenta color). **F** Comparison of reactivation strength (two-tailed paired t test, $n = 39$ trials from 6 mice, $t_{38} = -3.692$, $P = 0.000695$). **G** LFP and corresponding power spectrum during NREM sleep. Isolated theta waves are indicated by red rectangle box. **H** Distributions of mean duration of isolated theta waves. **I** Percentage of theta power during isolated theta wave and non-isolated theta wave phases (Wilcoxon Signed Rank Test, $n = 36$ channels from 6 mice, $Z = -5.243$, $P = 1.24 \times 10^{-7}$). **J, K** Coupling of isolated theta power and delta phase. **L** Distribution of isolated theta waves in relation to the delta phase. **M** Modulation index for normal and shuffled data (Wilcoxon signed-rank test, $n = 36$ channels from 6 mice during post-training NREM sleep, $Z = -5.232$, $P = 1.68 \times 10^{-7}$). **N** Raw LFP trace, corresponding power spectrum and reactivation strength (Rs.). Freq., frequency. **O** Distribution of reactivation events (R_T) during delta phase and a normal distribution fit to this distribution (red curve). **P** Theta power around the peak of reactivation strength. Inset, comparison of theta power in the period of R_T and baseline (Basal.) (Two tailed paired t test, $n = 39$ trials, $t_{38} = -8.998$, $P = 5.90 \times 10^{-11}$). *$P < 0.05$, **$P < 0.01$, ***$P < 0.001$. Data are presented as mean $\pm$ s.e.m. Source data are provided as a Source Data file.

burst-mode discharges lasting about hundreds of milliseconds during NREM sleep[23,36], which is possible to drive high-frequency oscillatory events in the neocortex. Additionally, RE has been reported to be involved in cortico-hippocampal interaction and is associated with memory performance[21,37,38]. Using retrograde neuronal tracing with red retrobeads, we further mapped the distribution of RE neurons projecting to the MEC and found that this cluster of neurons is mainly located in the RE from 0.46 to 1.82 mm post the bregma (Supplementary Fig. 4E–G). To further determine the connections between the RE and MEC, we injected AAV2/9-CaMKIIα-mCherry into the RE for anterograde tracing. Notably, the superficial layers of the MEC, rather than the deep layers of the MEC, contained a high density of mCherry-positive axonal fibers (Supplementary Fig. 4H, I), suggesting that MEC receives prominent inputs from the RE in the midline thalamic nuclei.

Next, we explored the correlation of the functional network activities between RE and MEC across different states in vivo by recording the LFP from both the RE and the superficial layers of the MEC. After analyzing the power spectrum of the LFP by wavelet transform, theta (4–12 Hz) waves in the RE recordings were also evident during NREM sleep (Fig. 2A–D). Coherence analysis further indicated that highest synchronized activity was observed in the theta band (5–7 Hz) between RE and MEC during NREM sleep (Fig. 2E). In contrast, the synchronized activity shifted to the gamma frequency band between these two brain areas when entering the resting and locomotor awake states (Supplementary Fig. 5), suggesting that RE inputs to the MEC may exhibit correlations with different network oscillations during distinct brain functional states. Furthermore, we conducted a Granger causality analysis to establish the temporal directionality between RE and MEC. Among the detected theta events during NREM sleep, the calculated F-value, which reflects the strength of the temporal directionality from RE to MEC, exceeded the critical value for most theta events (Supplementary Fig. 6). This indicates a clear temporal directionality from RE to MEC. Of note, the occurrence of theta oscillations in the hippocampus is primarily observed during movement and REM sleep. During locomotor awake states, the frequency of theta oscillations in the hippocampus was notably high, surpassing 8 Hz[39]. Conversely, synchronized theta activity between RE and MEC exhibited a lower frequency of less than 7 Hz, with these isolated theta oscillations being brief in duration lasting only a few hundred milliseconds. These findings indicate that isolated theta oscillations in MEC during NREM sleep possess distinct characteristics compared to those recorded during wakefulness.

What are the response properties of MEC cells to RE inputs that contribute to the isolated theta waves during NREM sleep? To test this, we further investigated the functional connections between RE and MEC by optogenetic stimulation (470 nm, 15 ms light pulse) of the RE afferents, combined with the patch-clamp recordings of the main excitatory neurons and inhibitory interneurons in the superficial layers of the MEC (Fig. 3A). These types of neurons could be distinguished by their morphology and electrophysiological properties (Fig. 3B, D, left). Optogenetic stimulation of the RE afferents reliably induced fast

excitatory postsynaptic currents (EPSCs) with short latency of 5.45 ± 0.23 ms and 5.19 ± 0.31 ms in 62.5% (15/24) of the excitatory neurons and 51.7% (15/29) of the inhibitory interneurons, respectively. These excitatory effects observed in the MEC diminished after block-ade of ionic glutamatergic receptors (Fig. 3B–E). These results, combined with the retrograde tracing data, imply the monosynaptic excitatory functional connections between the RE and MEC.

We also used different optogenetic stimulation frequencies (1, 5, 10 and 20 Hz) to observe the integration effect of the MEC cells on upstream inputs of RE. Under current-clamp model, 1 Hz, 5 Hz and 10 Hz optogenetic stimulation of the RE afferents resulted in reliably action potential firing in excitatory neurons, whereas 20 Hz stimuli induced a weaker increase in discharge frequency as compared 10 Hz. The efficiency of action potential generation in inhibitory interneurons is comparatively lower for stimuli of different frequencies compared to excitatory neurons (Fig. 3F, G). Consistently, using voltage-clamp mode to record the evoked EPSCs, we found that MEC cells exhibit distinct effects to different frequency stimuli of the RE afferents, with the strong integration to 5 Hz and 10 Hz stimuli, while the response to higher frequency (20 Hz) stimuli is weaker. As for different cell types, the response of excitatory neurons is much greater than that of inhibitory interneurons (Supplementary Fig. 7A, B). Together, these results indicate that MEC neurons efficiently integrate monosynaptic and excitatory inputs of RE in vitro.

Why do RE neurons and MEC inhibitory interneurons have a direct connection that does not efficiently produce action potential output in vitro? One possible explanation could be the absence of wakefulness-promoting neuromodulators, such as acetylcholine, which is widely distributed in the MEC-hippocampal circuit and strongly associated with spatial memory[6,40,41]. In isolated brain slices, this lack of neuromodulation leads to hyperpolarization and impairs the effective generation of action potentials. To verify this, we first depolarized the membrane potential of the interneurons with an average increment of 17.5 mV, in which case activating the RE afferents did induce significant action potentials in the MEC inhibitory inter-neurons (Fig. 3H–J). Furthermore, bath application of the wakefulness-promoting neuromodulator acetylcholine does significantly induce depolarization of the inhibitory interneurons in isolated brain slices, an effect that may enable these neurons to effectively respond to exo-genous excitatory inputs of the RE neurons (Supplementary Fig. 7C–E). In sum, these results imply that the RE may drive different functional activity patterns of MEC in different states. During NREM sleep, the level of wakefulness-promoting neuromodulators such as acetylcho-line is low, which may preferentially drive MEC to produce theta fre-quency network oscillations. In the awake state, on the other hand, the level of acetylcholine are higher, and it could efficiently excite the inhibitory interneurons. Given the important role of inhibitory inter-neurons in driving high-frequency network oscillations, such as gamma oscillations[42,43], it is likely that during the wake period, RE can drive MEC to produce higher frequency oscillations such as gamma oscillations during wakefulness.
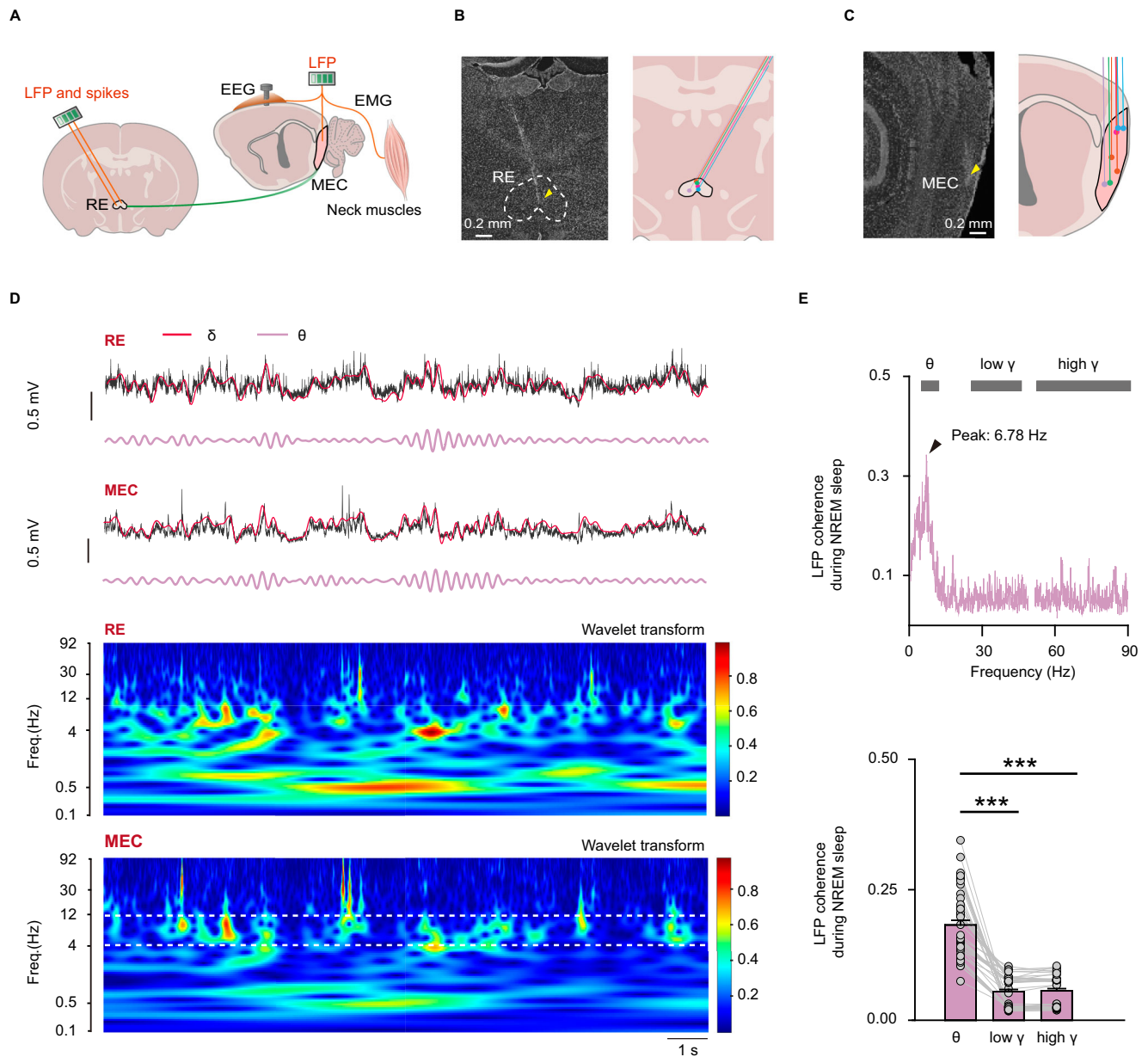
Fig. 2 | RE displays typical theta waves that synchronize with MEC theta oscillations. A Schematic of in vivo multi-channel synchronous recording in the RE and MEC, combined with EEG-EMG recording. **B**, **C** Images showing the electrode implanted in the RE (**B**) and MEC (**C**) ($n = 5$ mice). **D** Simultaneous recording of LFP (gray: raw trace; red: filtered delta; magenta: filtered theta) and corresponding power spectrum in the RE (top) and MEC (bottom) during NREM sleep. The range between two white dashed lines is the theta band in the MEC LFP power spectrum. **E** Diagram showing LFP coherence in different bands between RE and MEC during NREM sleep (top). Peak of LFP coherence (black arrowhead) is at the theta band. Comparison of LFP coherence in the RE and MEC during NREM sleep (bottom) (Friedman repeated measures ANOVA on ranks followed by post hoc Student–Newman–Keuls test, $n = 51$, theta vs low gamma: $q = 8.317$, $P = 1.55 \times 10^{-9}$; theta vs high gamma: $q = 6.832$, $P = 1.54 \times 10^{-9}$; low gamma vs high gamma: $q = -1.485$, $P = 0.412$). ***$P < 0.001$. Data are presented as mean ± s.e.m. Source data are provided as a Source Data file.

To further specifically investigate the correlation of the activities between of these two brain regions, we used photometry to selectively record the activity of the RE neurons projecting to MEC, and simultaneously recorded the LFP of the MEC (Fig. 4A, B). After the transitions from awakening to NREM sleep, the calcium (Ca^{2+}) activity of these RE neurons was significantly decreased (Supplementary Fig. 8A, B). In contrast, the Ca^{2+} activity of these cells was significantly increased after entering wakefulness from NREM sleep (Supplementary Fig. 8C, D). Although their activity decreased, the RE neurons projecting to MEC also exhibited discontinuous Ca^{2+} events during NREM sleep (Fig. 4C). The frequency of these Ca^{2+} activity events was increased, but the amplitude was significantly reduced, compared with the awake state

(Supplementary Fig. 8E, F). These results are consistent with previous reports that during NREM sleep the RE neurons still exhibit rhythmic burst-mode discharge[23,36]. Interestingly, when Ca^{2+} peaks appeared, reflected that neurons projecting to MEC were activated during NREM sleep, MEC exhibited strong theta wave activity (Fig. 4D–G), suggesting that the activity of this group of cells was positively correlated with the MEC theta event power.

We also specifically recorded the activities of RE neurons projecting to medial prefrontal cortex (mPFC) and hippocampal CA1, while simultaneously collecting LFP in the MEC (Supplementary Fig. 9A, G). Interestingly, neither the activity of RE neurons projecting to mPFC (Supplementary Fig. 9B–F) nor those projecting to the CA1
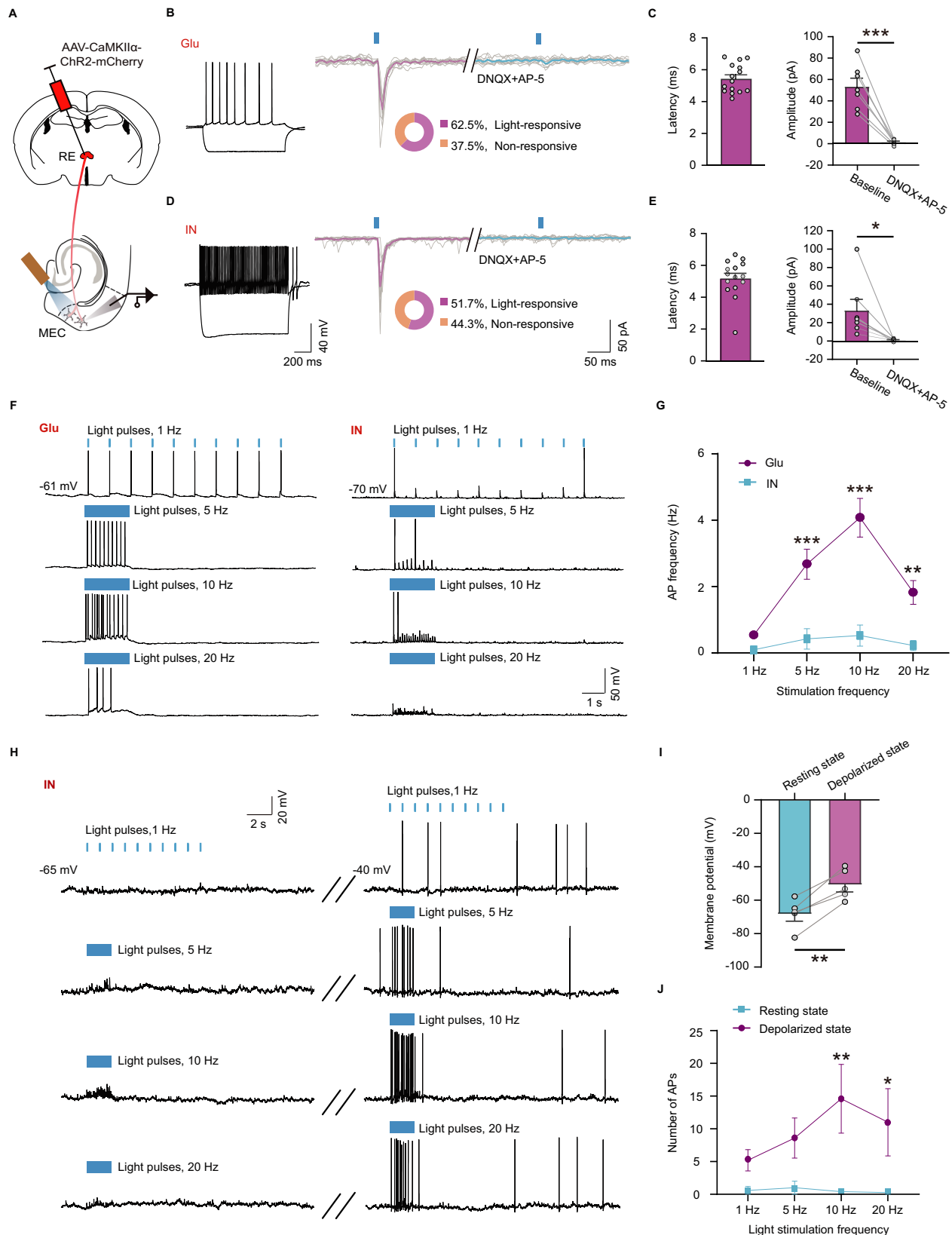
(Supplementary Fig. 9H–L) exhibited a positive correlation with MEC theta oscillations. These control experiments further support that only RE neurons projecting to MEC are specifically correlated with MEC theta oscillations.

In addition, if the isolated theta waves in the MEC originate from the RE inputs during NREM sleep, the spikes recorded in the RE should

be correlated with the theta waves in the MEC. To test this, a total of 104 cells were recorded from the RE, and on average, their discharge frequency during awakening was higher than that during NREM sleep (Supplementary Fig. 10A, B). Indeed, we found that the firing of 26% neurons was concentrated at a relatively fixed phase of delta waves-nested theta waves of the MEC during NREM sleep (Supplementary

Fig. 3 | MEC integrates monosynaptic excitatory inputs from RE neurons.
A Scheme for recording the evoked postsynaptic responses. **B** Left, electrophysiological property of glutamatergic neurons (Glu). Right, optostimulation evokes EPSCs in glutamatergic neuron in the presence (cyan trace) and absence (magenta trace) of DNQX and AP-5, and proportion of neurons that responded to stimulation of RE inputs. **C** Left, latency of glutamatergic neurons in response to light-stimulated RE inputs. Right, amplitude of the evoked EPSCs in the presence and absence of DNQX and AP-5 (Two tailed paired t test, $t_6 = 7.227$, $n = 7$ cells, $P = 0.0004$). **D** Same as (**B**) but for MEC GABAergic interneurons (IN). **E** Left, latency of MEC GABAergic interneurons in response to light-stimulated RE inputs. Right, same as (**C**) but for GABAergic interneurons (Wilcoxon signed-rank test, $n = 7$ cells, $Z = -2.336$, $P = 0.016$). **F** Sample traces showing responses of glutamatergic neurons (left) and GABAergic interneurons (right) to light pulses. **G** Frequency of action

potentials (AP) evoked by light pulses of glutamatergic neuron (magenta, $n = 10$ cells) and GABAergic interneuron (cyan, $n = 10$ cells) (Two-way Repeated Measures ANOVA followed by post hoc Bonferroni t test, Glu vs IN, $F_{1,18} = 21.045$, $P = 0.00131$; stimulation frequency factor, $F_{3,54} = 40.945$, $P = 3.48 \times 10^{-10}$; interaction, $F_{3,54} = 14.707$, $P = 7.18 \times 10^{-6}$). **H** Responses of GABAergic interneurons evoked by light pulses with voltage holding at -65 mV (left) or -40 mV (right). **I** Membrane potential of GABAergic interneurons when holding at resting states or depolarized states (two-tailed paired t test, n = 5 cells, $t_4 = -6.692$, $P = 0.0026$). **J** Number of action potentials evoked by light stimulation (Scheirer–Ray–Hare test followed by post hoc Holm-Sidak method, $n = 5$ cells; resting state vs. depolarized state, $H = 6.524$, $P = 7.51 \times 10^{-11}$; stimulation frequency factor, $H = 0.125$, $P = 0.632$; interaction, $H = 0.183$, $P = 0.48$). $*P < 0.05$, $**P < 0.01$, $***P < 0.001$. Data are presented as mean ± s.e.m. Source data are provided as a Source Data file.

Fig. 10C–E). These results imply the activation of RE neurons may contribute to the isolated theta waves during NREM sleep.

RE triggers isolated theta waves-related memory reactivation

The overarching aim of this project was to elucidate the underlying mechanisms responsible for the reactivation of the MEC cells. The data so far pointed to the need to change our focus to the RE neuron projections to the MEC as likely mediator of this role, because of the correlation between the RE activity and the MEC isolated theta waves during NREM sleep. To test this, we chemogenetically inhibited RE-MEC pathway by injecting AAV2/9-CaMKIIα-hM4D-mCherry or AAV2/9-CaMKIIα-mCherry as control into the RE combined with implantation of cannula into the MEC (Fig. 5A). In vitro patch-clamp recordings of the RE neurons expressing hM4D-mCherry validated that Clozapine N-oxide (CNO) significantly inhibited neuronal firing rates (Fig. 5B, C). The application of CNO also significantly reduced the firing frequency of MEC cells, accompanied by a specific decrease in the frequency of spontaneous excitatory postsynaptic currents (sEPSCs) while leaving the amplitude of sEPSCs unaffected (Supplementary Fig. 11). These findings demonstrate the efficacy of this chemogenetic approach. After the mice were trained in the six-arm maze, CNO (5 μM) was injected immediately into the MEC to inhibit the RE-MEC pathway in vivo (Fig. 5D–F). Chemogenetic inhibition of this pathway can remarkably prolong the distance to find the target arm and increase the number of errors entering the non-target arms (Fig. 5G–I), indicating the impairment of spatial memory consolidation after inhibition of this pathway.

Although chemogenetic inhibition demonstrated the necessity of RE-MEC pathway in spatial memory consolidation, it is not yet clear whether this pathway affects memory consolidation by affecting the isolated theta waves and replay of the MEC cells. On this basis, we further adopted closed-loop optogenetic approach to specifically trigger the inhibition of RE-MEC pathway following a few milliseconds of the isolated theta wave detection during NREM sleep (Fig. 6A). Closed-loop optogenetic interventions were performed by selectively expressing the ArchT3.0 fused to eYFP or eYFP alone in the MEC-projecting RE neurons (Supplementary Fig. 12A, B). Once a theta event was detected, yellow laser (300 ms, 20 mW) was triggered to inhibit RE-MEC pathway. The duration of 300 ms yellow laser stimulation was selected primarily based on the fact that the average duration of theta events was ~300 ms. Closed-loop optogenetic inhibition of the RE-MEC pathway effectively reduced theta wave power (Supplementary Fig. 12C, D), decreased the coupling strength of the delta wave and isolated theta waves during NREM sleep, and altered the preferred phase in which isolated theta waves are coupled to delta waves (Fig. 6B–D).

In parallel, closed-loop optogenetic inhibition of the RE-MEC pathway caused a remarkable decrease in the reactivation strength of the learning-related MEC cell ensembles during the subsequent NREM sleep (Fig. 6E–G). At the behavioral level, closed-loop optogenetic

inhibition caused impairment of spatial memory consolidation, reflected by prolonged distance to find the target arm and the increases in the number of errors entering the non-target arms (Fig. 6H–J). Optogenetic manipulation of RE-MEC pathway had no effects on post-training sleep-wakefulness architecture and EEG power spectrum (Supplementary Fig. 12E–I), which ruled out the impairment of memory consolidation caused by the change of sleep–wake state.

Considering that RE projections can also extend to the mPFC, we aim to investigate the impact of RE inputs on network oscillations of the mPFC during NREM sleep. After optogenetic inhibition of the RE-mPFC pathway, there was a significant reduction in beta and gamma oscillations, while theta oscillations remained unaffected (Supplementary Fig. 13A–D). In control animals, light stimulation did not affect neuronal network oscillatory activity in the mPFC (Supplementary Fig. 13E, F). These findings suggest that RE may participate in memory consolidation through distinct network oscillation mechanisms in different cortical regions during NREM sleep.

Discussion

The interplay of triple cardinal rhythms, including neocortical SO, thalamo-cortical spindles and hippocampal ripples, is thought to initiate the systematic consolidation of spatial memory during NREM sleep. The hierarchical coupling provides a temporally fine-tuned framework for information redistribution from temporary to long-term storage sites[11,44,45]. Using timed electrical stimulation in rats, reinforcing the endogenous temporal coordination of triple-coupling can enhance the retainment of spatial memory[46]. In contrast, disrupting these couplings impairs subsequent memory recall, implicating their causal role in memory information consolidation[47,48]. The present study reports that reactivation of learning-related MEC cell assemblies occurs in transient delta waves-nested isolated theta waves during NREM sleep following a spatial memory task. These results reveal another type of network oscillatory dynamics linking to memory reactivation during NREM sleep (Supplementary Fig. 14), which implies that different brain regions may adopt distinct network oscillatory mechanisms to coordinate the reactivation of memory traces. However, it is not yet known whether this form of oscillatory dynamics in the MEC operates independently or synergistically with hippocampal SWRs and neocortical SO-nested spindles.

We found that MEC receives dense projections from the RE of the midline thalamus, which is consistent with the previous report[49]. RE serves as the major anatomical route between the mPFC and hippocampus, and has been shown to be critical for spatial working memory[50]. RE inactivation decreased working memory specific theta synchrony between the mPFC and dorsal hippocampus[25], and impaired spatial working memory[25,51]. Some evidence also suggests that RE may be involved in the consolidation of spatial memory; however, these results are still contradictory[38]. The lesions of ventral midline thalamus including RE with excitotoxic N-methyl-D-aspartic acid did not impact the recent memory recall, while the long-term memory performance
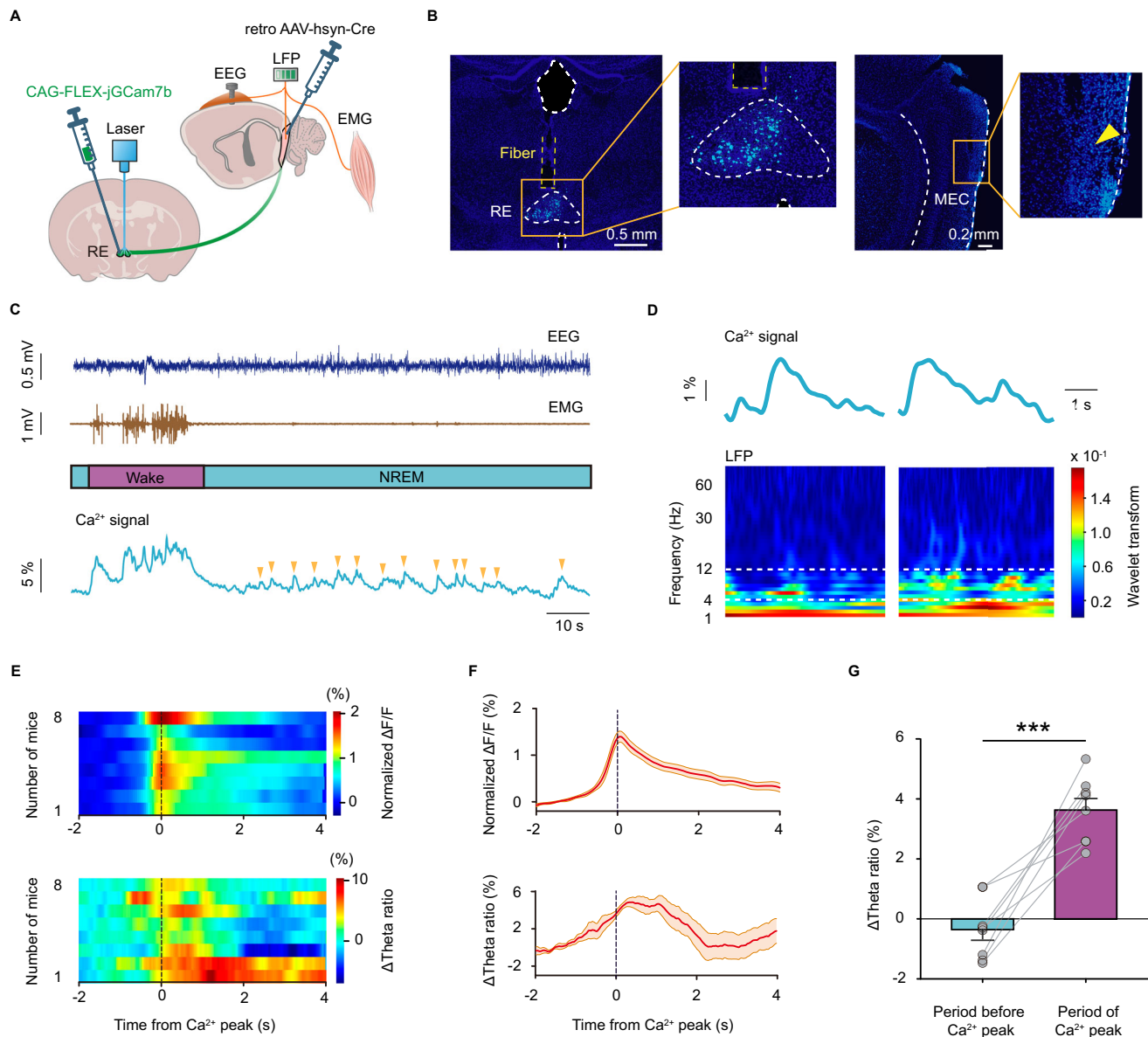
Fig. 4 | MEC isolated theta waves are positively correlated with increase in the activities of RE neurons projecting to the MEC. A Diagram for simultaneously fiber photometry recording of RE neurons projecting to MEC as well as LFP recordings in the MEC. **B** Representative image showing the expression of jGCamp7b (green) and the optical fiber (dotted yellow pane) implanted in the RE (left) and the electrode implanted in the MEC (right, yellow arrowhead), and related enlarged view. **C** Representative raw EEG-EMG traces, color-coded hypnogram, and Ca^{2+} signals from a RE-MEC^{jGCamp7b} mouse. **D** Two examples showing synchronous recordings of Ca^{2+} activity of RE neurons projecting to MEC (top) and LFP in the MEC (bottom) during NREM sleep. Between two dotted white lines is theta frequency band (4–12 Hz). **E** Heatmaps illustrating synchronous change of Ca^{2+} activity of RE neurons projecting to MEC (top) and increment of theta/(delta + theta) ratio (ΔTheta ratio, bottom) around Ca^{2+} peak (0 s) during NREM sleep ($n = 8$ mice). **F** Average value of synchronous change of Ca^{2+} activity (top) and ΔTheta ratio (bottom) from 8 mice displayed as (**E**). Data are presented as mean (red line) ± s.e.m. (shaded area). **G** Statistic analysis of ΔTheta ratio before and during the period of Ca^{2+} peak (two-tailed paired t test, $n = 8$ mice, $t_7 = -6.672$, $P = 0.000285$). ***$P < 0.001$. Data are presented as mean ± s.e.m. Source data are provided as a Source Data file.

was impaired after training[21]. Additionally, some results point to the RE as a functional hub able to finely coordinate hippocampal-prefrontal gamma bursts during slow oscillations and slow-wave activity, which have been reported to be associated with memory consolidation[37,52]. In contrast, other studies indicated a preferential role of the RE in retrieval rather than in consolidation, because systematic inactivation of the RE after each learning session did not alter the acquisition of the task or remote memory performance 20 days later in an elevated crossword-like maze[53]. The discrepancy in these previous work might be explained by a lack of recording and specific manipulation of neuronal activity in the RE during the consolidation stage post spatial memory encoding.

In the present study, we demonstrate that RE exhibits prominent theta waves, which are highly synchronized with those occurring in the MEC. The neuronal activity of the RE is also positively correlated with the isolated theta waves of the MEC during NREM sleep. Specific
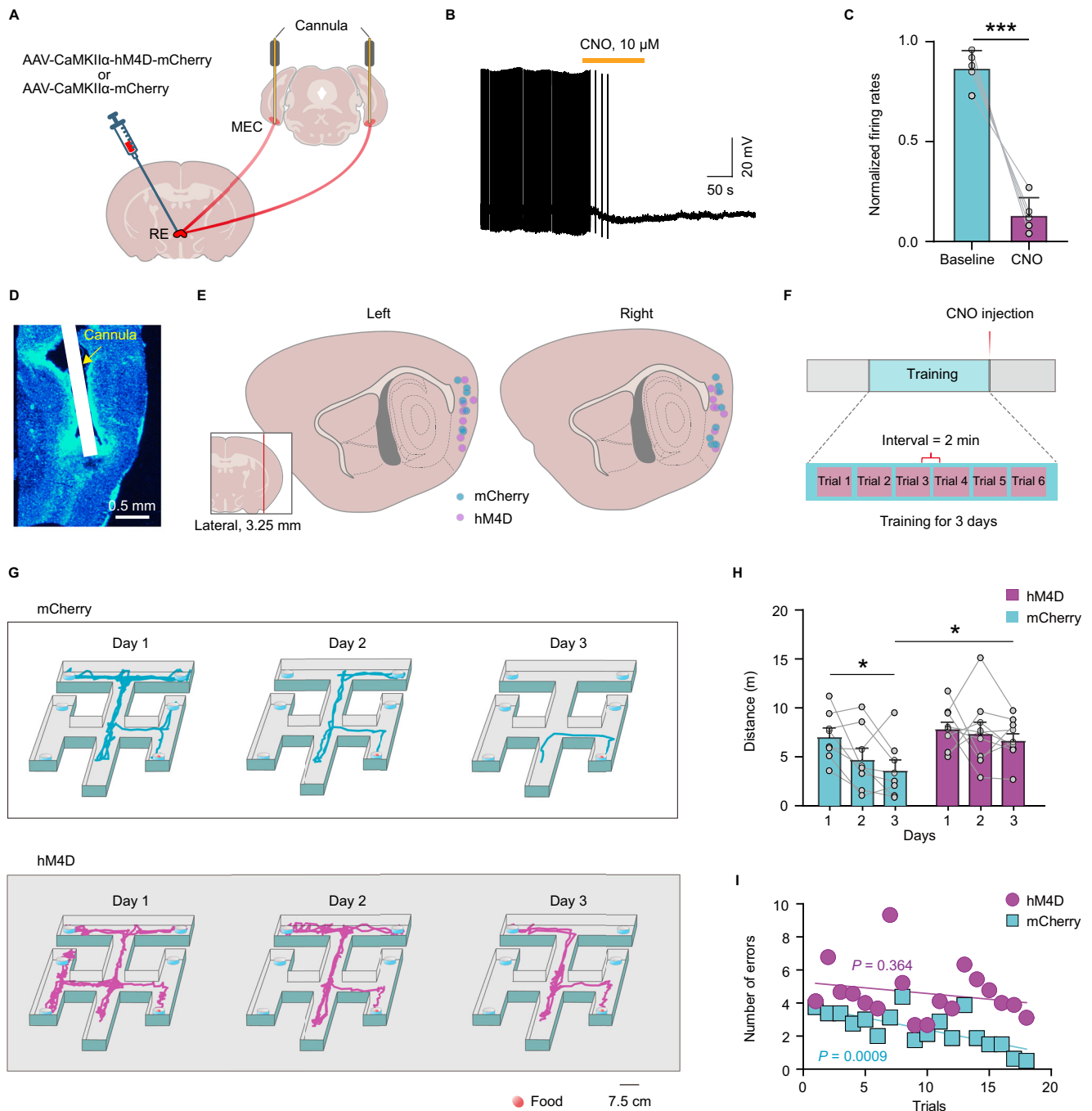
Fig. 5 | Chemogenetic inhibition of RE-MEC pathway after training impaired spatial memory. A Schematic of chemogenetic inhibition of RE-MEC pathway. **B** Representative trace showing the inhibitory effect of CNO (10 μM, 2 min) on the firing activities of an example hM4D-expressing RE neuron projecting to MEC. **C** Bath application of CNO suppressed the firing rates of the RE neurons (Two tailed paired t test, $t_4 = 9.396$, $n = 5$ cells, $P = 0.000715$). **D** Representative sagittal section showing the cannula implanted in the MEC. **E** Microinjection sites were depicted as filled cyan (mCherry) or magenta (hM4D) circles for the tested mice. **F** Experimental design of CNO-induced chemogenetic inhibition of RE-MEC pathway combined with the spatial memory task. **G** Representative trajectories of the mice in the mCherry (top) or hM4D (bottom) group searching for food in the six-

arm maze. **H** The distance that animals of the mCherry and hM4D groups traveled in the maze to acquire food each day (two-way repeated measures ANOVA followed by post hoc Bonferroni t test, $n = 8$ mice for mCherry group, $n = 9$ mice for hM4D group; mCherry vs hM4D, $F_{1, 15} = 4.696$, $P = 0.047$; days factor: $F_{2, 30} = 4.510$, $P = 0.019$; interaction, $F_{2, 30} = 1.194$, $P = 0.317$). **I** Average number of errors that animals in the mCherry and hM4D groups made when searching for food during 6 trials each day. Cyan circles or magenta blocks represent mean value for each trial of mCherry ($n = 8$ mice) or hM4D group ($n = 9$ mice). Trend lines are the least-square fits to the data. *$P < 0.05$, ***$P < 0.001$. Data are presented as mean ± s.e.m. Source data are provided as a Source Data file.

suppression of projections from the RE to MEC resulted in disruption of these delta waves-nested theta waves, decreased reactivations of spatial learning-related MEC cell assemblies and deterioration of spatial memory consolidation. The findings highlight the role of the RE in the midline thalamus in driving isolated theta waves and temporally

driving memory reactivation in the MEC, thereby further elucidating the neural circuitry mechanisms underlying memory consolidation during NREM sleep.

During the wake-sleep cycle, different network oscillatory activities occur in the hippocampal-entorhinal circuit to mediate the
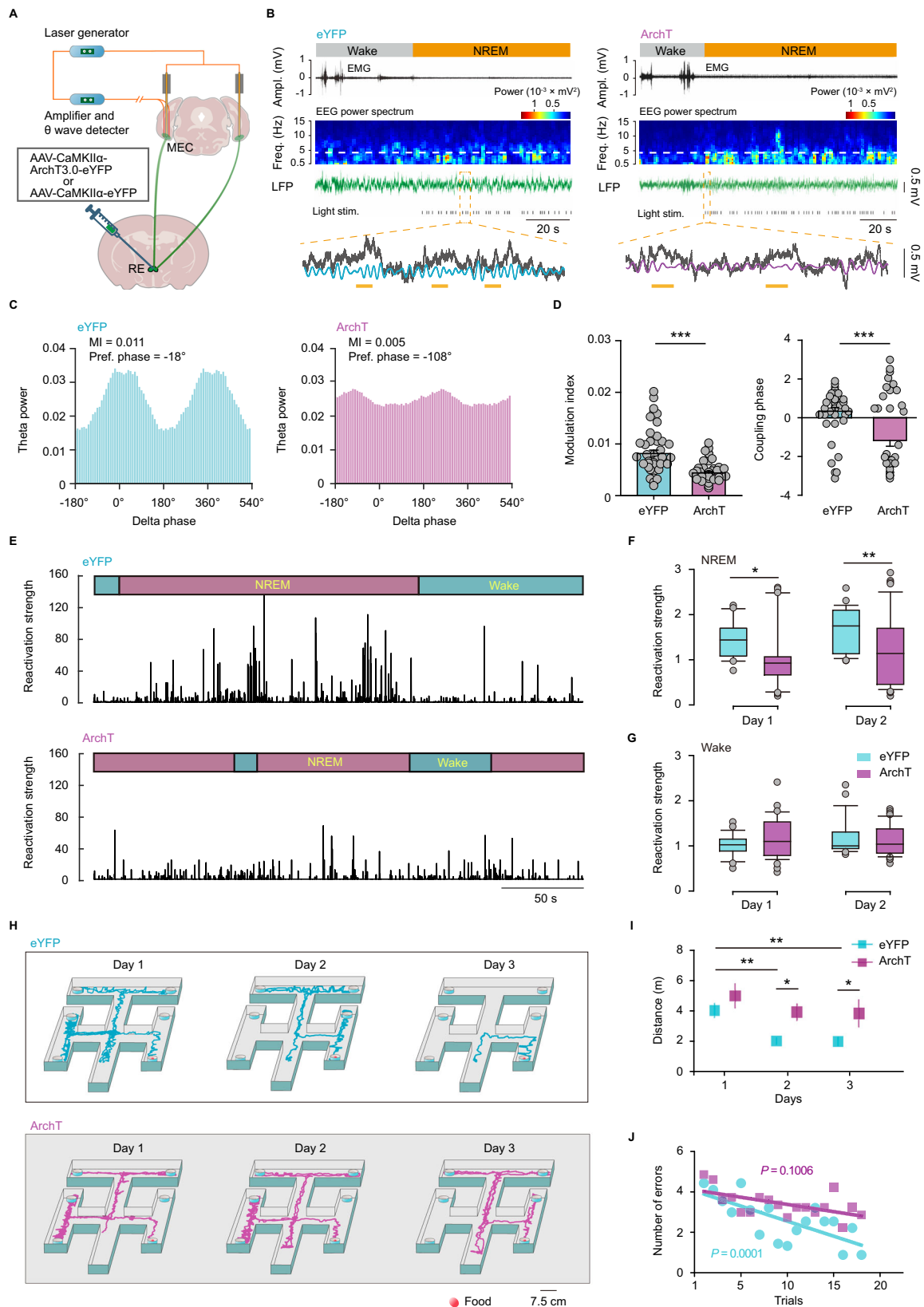
routing and processing of memory information. During active wakefulness, this neural circuit mainly displays theta oscillations, and nested high-frequency gamma events to help realize memory encoding and retrieval[3]. After entering to NREM sleep phases, the MEC shows low-frequency delta oscillations in which isolated theta waves are nested, while the hippocampus shows typical SWRs, which contributes

to the restorative functions of sleep and systematic memory consolidation[54,55]. The RE exhibits distinct characteristics in comparison to the hypocretinergic and cholinergic neuromodulatory systems, as RE neurons maintain rhythmic firing patterns even during NREM sleep[37,52]. The aforementioned statement implies that RE enables the initiation of memory engram cell reactivation, thereby leading to

Fig. 6 | RE triggers isolated theta waves required for memory consolidation.
A Schematic of closed-loop optogenetic inhibition. **B** Representative EMG traces, EEG power spectrum and LFP. Enlarged view shows LFP (gray), filtered LFP in theta band (Cyan: eYFP group; magenta: ArchT group). Ampl. amplitude, Freq. frequency, Light stim. light stimulation. **C** Theta power-delta phase coupling. M.I. modulation index, Pref. phase preferred phase. **D** Modulation index (left, Mann−Whitney rank-sum test, eYFP: $n = 44$, ArchT: $n = 42$, $U = 364$, $P = 1.00 \times 10^{-6}$) and phase (right, Welch's t test, eYFP: $n = 44$, ArchT: $n = 42$, $t_{69.535} = 4.320$, $P = 5.08 \times 10^{-5}$) of theta-delta wave coupling. **E** Reactivation strength of the eYFP and ArchT group. **F** Boxplots showing reactivation strength during NREM sleep. Boxplots represent median plus minima and maxima with lower and upper quantiles; whiskers, one and a half times of interquartile range; points, outliers

(Kruskal−Wallis one-way ANOVA on ranks, $H = 21.403$, $P = 8.7 \times 10^{-5}$; Day 1: eYFP: $n = 27$, ArchT: $n = 38$, $H = 3.004$, $P = 0.016$; Day 2: eYFP: $n = 28$, ArchT: $n = 49$, $H = 3.189$, $P = 0.008$). **G** Same as **F** but for post-training wakefulness (Kruskal−Wallis one-way ANOVA on ranks, $H = 1.653$, $P = 0.647$; Day 1: eYFP: $n = 27$, ArchT: $n = 38$, Day 2: eYFP: $n = 28$, ArchT: $n = 49$). **H** Representative trajectories in eYFP and ArchT group. **I** Distance traveled in the maze (Two-way Repeated Measures ANOVA following post hoc Fisher LSD Method, eYFP: $n = 9$ mice, ArchT: $n = 8$ mice. eYFP vs. ArchT, $F_{1,15} = 5.706$, $P = 0.030$; days factor, $F_{2, 30} = 8.284$, $P = 0.001$; interaction, $F_{2, 30} = 0.720$, $P = 0.495$). **J** Cyan circles or magenta blocks represent average number of errors of eYFP ($n = 9$ mice) or ArchT group ($n = 8$ mice). Trend lines are the least-square fits to the data. *$P < 0.05$, **$P < 0.01$, ***$P < 0.001$. Data are presented as mean ± s.e.m. Source data are provided as a Source Data file.

memory consolidation. Undoubtedly, these findings have further expanded our understanding of midline thalamus in memory consolidation, and provide a target in the treatment of memory disorders.

The different network oscillation patterns of hippocampus and MEC, correlated with NREM memory reactivation, may be due to their distinct functional properties. It has been reported that the layer III of MEC exhibits presistent firing activity lasting several hundred milliseconds. Additionally, our results indicate that MEC neurons more efficiently integrate excitatory inputs from RE at theta frequency band in vitro. These functional properties of MEC may enable it to participate in memory consolidation through a unique mechanism of isolated theta waves. Of note, although the in vitro patch-clamp experiment revealed that RE strongly excites MEC excitatory neurons, it is important to consider that interneurons receive a substantial amount of input from local excitatory glutamatergic neurons within the MEC region[56]. Therefore, the reactivation of excitatory neurons triggered by RE input during NREM sleep may subsequently drive the reactivation of interneurons through this local circuit in the MEC in vivo.

Previous studies have recorded ensembles of grid cells in superficial layers of MEC during active exploratory behaviors and NREM sleep. The patterns of spike-time correlations that reflected the spatial tuning offsets between these grid cells during active exploration was also observed during the NREM sleep[57]. The current study primarily employed a six-arm maze behavioral paradigm to investigate MEC-related spatial memory, which may not be optimal for detecting grid cells. Further investigation is required to determine whether the identified isolated theta oscillations drive the reactivation of grid cells during NREM sleep.

Methods
Animals
Wild-type *C57BL/6* mice (8−12 weeks old) were used in this study. The experiments involved the use of male mice for multi-channel single-unit and Ca^{2+} signal recordings, behavioral tests including the spatial memory test with optogenetic manipulation of RE-MEC pathway, as well as morphological experiments. All the animals (4−5 mice in a cage) were kept in the animal experiment center of Army Medical University with stable ambient temperature of $24 \pm 1\,°C$ and the feeding house was kept on a 12/12 h light/dark cycle (lights on at 8:00 A.M.). The mice that underwent fiber or cannula implantation surgery need to be housed separately. All the experiments were in line with the ethical requirements for animal care and use of Army Medical University and the procedures were approved by the ethics committee of Army Medical University.

Surgery
Wild-type mice were anesthetized under 1% isoflurane and placed in a stereotaxic instrument (RWD Life Technology, China). Erythromycin eye ointment was applied to prevent corneal drying and light injury. An incision was made in the scalp, the head was leveled, and bregma coordinates were identified. A small drill hole (0.5×0.5 mm) was

drilled at the skull corresponding to the coordinates of the RE (AP = −0.8 mm, ML = +1.0 mm, DV = −4.0 mm, tilt +15°), MEC (AP = −4.4 mm, ML = ± 3.8 mm, DV = +1.9 mm), mPFC (AP = 1.8 mm, ML = 0.5 mm, DV = 1.5 mm) and ventral CA1 (vCA1) (AP = −3.1 mm, ML = ± 3.2 mm, DV = 3.5 mm) for injections of viruses. The glass pipette was used for virus micro-injections. After arriving at the target area, the pipette was kept in site for 2 min. The pipette was held in place for 10 min, and then withdrawn slowly.

For retrograde tracing experiment, RV-N2C(G)-ΔG-dsRed (400 nL, BrainVTA, China) or red retrobeads (400 nL, Lumafluor) was bilaterally injected into the MEC. AAV2/9-CaMKIIα-mCherry (200 nL, BrainVTA, China) was injected into the RE (200 nL, BrainVTA, China) for anterograde tracing experiment.

For the fiber photometry recording activities of RE neurons projecting to MEC, AAV2/9-CAG-FLEX-jGCamp7b (200 nL, Taitool Bioscience Co. Ltd, China) was injected into RE, and AAV2/2Retro-hSyn-Cre (400 nL, Taitool Bioscience Co. Ltd, China) was bilaterally injected into the MEC. For the brain region control experiments, AAV2/9-CAG-FLEX-jGCamp7b (200 nL) was injected into the RE, and AAV2/2Retro-hSyn-Cre (400 nL) was bilaterally injected into the mPFC or vCA1. After 2 weeks, optical fiber (OD = 200 μm, NA = 0.37, Inper, China) was implanted into the RE. Meanwhile, the electrode used for LFP recording was implanted in the MEC.

For the closed-loop optogenetic stimulation experiments, AAV2/9-CaMKIIα-ArchT3.0-eYFP (BrainVTA, China) or AAV2/9-CaMKIIα-eYFP (control, BrainVTA, China) were injected into the RE with a total volume of 200 nL. After 2 weeks, the optic fibers surrounded by electrodes were bilaterally implanted into the MEC for light delivery and electrophysiological recordings. Similar procedures were adopted to inject 200 nL AAV2/9-CaMKIIα-ChR2-mCherry (Obio, China) into the RE for patch-clamp experiments. And in the optogenetic inhibition of RE-mPFC experiment, same strategy for virus injection was carried out, while the optoelectrode was unilaterally implanted into the right mPFC.

For designer receptors exclusively activated by designer drug experiments, AAV2/9-CaMKIIα-hM4D-mCherry (BrainVTA, China) or AAV2/9-CaMKIIα-mCherry (control, BrainVTA, China) into the RE with a total volume of 200 nL. After 2 weeks, the cannula (L = 5 mm, ID = 0.25 mm, RWD Life Technology, China) was bilaterally implanted into the MEC, and a stainless-steel dummy cannula (ID = 0.2 mm, RWD Life Technology, China) was inserted into the guide cannula.

To explore the characteristics of MEC firing activity, the electrode array was unilaterally implanted into the MEC. Similarly, to investigate the correlation between RE and MEC electrophysiology activity, the electrode arrays were implanted into the RE and unilateral MEC for spikes and LFP recording. For EEG and EMG recordings, two screws into the skull on top of the left and right cortex was inserted on the surface of mPFC. A reference screw was inserted into the skull on top of the cerebellum. Also, one EMG electrode was fixed into the dorsal neck musculature. All the optical fibers, cannula or electrodes inserted were affixed to the skull with dental cement. The placement

coordinates of the optical fiber, cannula or electrodes was the same as described above in the virus injection sections. And animals after surgery were allowed to recover for 7 days and at least 3 weeks to express the viruses before the behavioral testing.

Behavioral apparatus and training procedure

Six-arm maze was used in all behavioral sessions. The maze consisted of four crossing stem arms and six side arms. Each arm (30 cm long, 8 cm wide and 17.5 cm high) was made by 3–4 milky acrylic plates (0.5 cm in thickness). The tops of the arm were open to allow tracking of the animal inside. Four figures of different shapes (star, square, circle, triangle) were attached on both sides of walls of two stem arms perpendicular to the entrance arm.

Three days before training, animals were placed on food restriction (80–90% of initial weight) and kept at 25 °C room. During the training days, the mouse was fed with 2–2.5 g of food per day to maintain body weight. One day before formal training, then the animal was exposed to the maze twice for adaptive exploration. Before entrance, pellets (50 mg) were placed in the container at the end of six side arms, then the animal was put in and trained to retrieve food. After going through all the arms and collecting all the pellets, the subject was gently taken out and placed in its homecage. Once animal was habituated to the maze and started consuming the pellets, it entered the formal training phase next day.

Training procedure involves three consecutive days of spatial learning in the maze. The learning session consisted of six trials and 2 min interval between each trial. In each trial, pellet was always placed in the container of the fixed arm. Then the animal was put in the maze to search for the pellet. Once the rewards had been consumed, the near board was lifted, and the mouse was gently guided back to the homecage for a 2-min rest. After that trial procedure was repeated six times, the mouse was immediately placed in its homecage for post-training 1-h sleep recording. To prevent the use of an odor-guided search strategy during these experiments, the board was periodically wiped. In addition, trials with immobility longer than 1 min were excluded.

Multi-channel single-unit recording

For the in vivo recording the spikes and LFP, a custom-made electrode array was used. The electrode array consisted of 3 tetrodes and 2 wires for EEG-EMG recording. A tetrode was made up of 4 insulated nickel-cadmium wires (100–250 kΩ, California Fine Wire) twisted together. The electrode was slowly lowered into the target region with the help of brain stereotaxic apparatus (RWD Life Technology, China). Reference electrodes were fixed above the cerebellum with small stainless screws. The electrode was tightly cemented on the animal's skull. Electrodes were connected to a 16-channel headstage (30 kHz, Neuralynx) with an amplifier for each wire and a green LED (3 V) for tracking the position of the animal. The headstage was connected to a 2 m cable plugged into a commutator that allows the animal to move freely in the behavioral task. Signals were amplified (Digital Lynx SX; Neuralynx, MO, USA) and acquired by Cheetah 5.7.4 acquisition software (Neuralynx). Units were amplified 10,000 times using a 16-channel amplifier (Neuralynx) and band-pass filtered at 300–10,000 Hz. Wild band signals were digitized at 30 kHz and band-pass filtered (0.1–9 kHz) by an amplifier (Digital Lynx SX; Neuralynx, MO, USA).

Optogenetic intervention

As for closed-loop optogenetic inhibition of RE-MEC pathway, the bilateral optical fibers of MEC were connected to the 589 mm yellow laser generator (Newdoon Technology Co. Ltd., China). A closed-loop system was used for real-time optogenetic intervention. Finishing 6-trials spatial learning, mice were placed in the homecage for 1-h sleep recording by Cheetah 5.7.4 acquisition software (Neuralynx), as well as in real-time LFP recording in the MEC with the Neuralynx Hardware

Processing Platform. Transistor-Transistor Logic (TTL) pulse high time was set at 300 ms and the detection lockout time was set at 500 ms. TTL pulse was selectively transmitted only when the peak of theta power exceeded one standard deviation from the average theta activity[58]. Once theta wave was detected during post-training NREM sleep, yellow laser (300 ms, 20 mW) was triggered by TTL pulse procedure to inhibit RE-MEC pathway.

The subject mouse was returned to the home cage immediately and the EEG-EMG recording was monitored to manually identify NREM episodes across the following 1 h. NREM sleep was defined by high amplitude and low-frequency EEG activity, as well as low amplitude EMG activity. Once the mice entered NREM sleep, the laser generator was turned on, and the closed-loop system would specifically detect theta oscillations during NREM sleep to trigger the optogenetic stimulation. The 93.8% and 90.5% of optogenetic stimulation were applied during NREM sleep on day 1 and day 2 in the mice with RE expressing ArchT3.0-eYFP.

For optogenetic inhibition of the RE-mPFC pathway, unilateral optical fiber of mPFC was connected to the 589 mm yellow laser generator (Newdoon Technology Co. Ltd., China). Mice were placed in the homecage for 1–2 h sleep recording (Neuralynx), as well as in real-time LFP recording in the mPFC with the Neuralynx. A light stimulation lasting for a duration of 20 s when the mice entered stable NREM sleep, as evidenced by consistent EEG pattern. At the distal end of the optical fiber the laser intensity was set to 15 mW under consistent illumination.

Chemogenetic intervention

For the chemogenetic inhibition experiment, CNO (500 nL, Tocris, USA) was bilaterally delivered into the MEC through an intracranially-inserted cannula, immediately after training session each day. A syringe pump (Harvard apparatus) was used for infusion at a rate of 250 nL/min. The needle was held in place for another 2 min, and then withdrawn slowly.

Fiber photometry recording

To perform the fiber photometry recording experiment, a commercialized fiber photometry system (Inperstudio Alpha 8.2, Inper, China) was used to record RE Ca^{2+} signals. An optical fiber (200 μm in diameter, NA of 0.37, Inper, China) was used to guide the laser from the optical commutator to the implanted optical fiber. A 470 nm and a 410 nm laser beam were used for excitation and isosbestic wavelength, respectively. The laser power at the tip of the optical fiber was set at 20–30 μW (470 nm) and 10–20 μW (410 nm) to minimize photobleaching. The 410-nm channel was used as an isosbestic control. The fluorescence signals were bandpass filtered and collected by a photomultiplier tube. The current signals from the photomultiplier tube were converted to voltage signals by an amplifier, which was further filtered through a low-pass filter. The analogue voltage signals were digitalized at 20 Hz, and recorded by fiber photometry software (Inperstudio Alpha 8.2, Inper, China). Meanwhile, Bayonet Neill-Concelman was used to connect the fiber photometry system and multi-channel single unit recording system for synchronous recording neural activities. After triggering the start of synchronous recording in the Inper Signal software, 40 min of Ca^{2+} signals of RE neurons projecting to MEC and LFP in the MEC were recorded as well as EEG-EMG recording.

Whole-cell patch-clamp recording

The whole-cell patch-clamp recordings procedures were consistent with previous studies[59–61]. Mice were decapitated after being anesthetized with isoflurane. The brain was rapidly removed and placed into the ice-cold section solution oxygen-saturated with 95% O_2 and 5% CO_2. The section solution was composed of 220 mM sucrose, 10 mM glucose, 2.5 mM KCl, 1 mM $CaCl_2$, 26 mM $NaHCO_3$, 6 mM $MgCl_2$ and 1.25 mM NaH_2PO_4. The brain was cut into horizontal slices containing

the MEC with 400 μm thickness in the ice-cold section solution by a VT1000 tissue slicer (Leica, Germany) and then incubated for 1 h in the oxygen-saturated artificial cerebrospinal fluid (ACSF) containing 2.5 mM KCl, 125 mM NaCl, 2 mM $CaCl_2$, 26 mM $NaHCO_3$, 1.3 mM $MgSO_4$, 1.25 mM NaH_2PO_4, 20 mM glucose at room temperature. Then, the brain slices were moved into a submerged chamber for recording with continuous infusion of oxygen-saturated ACSF.

The targeted neurons were identified by an upright fluorescent microscope (Olympus, Japan) equipped with differential contrast optics and an infrared video imaging camera. The whole-cell recordings were conducted on the target neurons in the MEC with glass pipettes containing the solution (130 mM potassium gluconate, 5 mM KCl, 2 mM $MgCl_2$, 10 mM HEPES, 0.1 mM EGTA, 2 mM Na_2-ATP, 0.2 mM Na_2-GTP). After clamping the targeted neurons at −60 mV with stable recoding for at least 15 min, step currents (−300 pA to +300 pA, Δcurrent = 100 pA, duration = 1 s) were injected into the clamped neurons to induce voltage curves and action potentials. Different neuronal types were distinguished by the morphological and electrophysiological properties of these neurons. The excitatory glutamatergic neurons exhibited larger somata and smaller fast afterhyperpolarization potential. While the interneurons showed fast afterhyperpolarization potential and faster spike firing rates.

To stimulate ChR2 expressed in axon terminals from the RE, AAV2/9-CaMKIIα-hChR2(H134R)-mCherry (Obio Technology Co. Ltd., China) were injected into the RE of the adult mice. After about 4 weeks of virus expression, glutamatergic neurons and interneurons were recorded from the horizontal brain slices containing the MEC, which were prepared according to the above-mentioned method. To demonstrate whether monosynaptic functional connection is established between RE and MEC neuron, the postsynaptic effect of MEC neurons were recorded under the voltage clamp configuration. After a stable baseline recording, 473 nm blue light (1 Hz, 15 ms, 10 mW under constant light) was delivered to evoke excitatory postsynaptic effects via an optical fiber placed above the recorded cell. Then, 6,7-dinitroquinoxaline-2,3-dione (DNQX, 10 μM) and d-(−)−2-amino-5-phosphonopentanoic acid (AP5) (50 μM) was used to block action potential-based excitatory monosynaptic transmission under blue light.

To evaluate the integrated strength of MEC neurons in response to RE inputs, a series of light pulses (1 Hz, 5 Hz, 10 Hz, 20 Hz) were applied to stimulate RE axon terminals in the MEC. The responses of glutamatergic neurons and interneurons in the MEC were recorded under the voltage and current clamp configuration. The light pulses were applied under the control of an eight-channel programmable pulse stimulator (Master-8, A.M.P.I. USA). Parameters of light pulses: 1 Hz: duration = 15 ms, interval = 1 s, M = 10; 5 Hz: duration = 15 ms, interval = 200 ms, M = 10; 10 Hz: duration = 15 ms, interval = 100 ms, M = 20; 20 Hz: duration = 15 ms, interval = 50 ms, M = 40. To verify when RE-MEC^{GABA} pathway is activated, MEC interneurons were clamped at resting and depolarized potentials. And a series of light pulses (1 Hz, 5 Hz, 10 Hz, 20 Hz) were applied to stimulate terminals from RE to observe whether action potentials of recording cell were effectively evoked under current clamp mode. The mean amplitude of EPSCs induced by each stimulus was calculated to evaluate the response of MEC neurons to different frequency stimulation of RE inputs.

Wakefulness-promoting neurotransmitter acetylcholine (MCE, China) was also added to observe its effects on the MEC interneurons. The interneurons were recorded as baseline states with membrane potentials held at resting states under current clamp mode. Following 15 min of baseline recording, acetylcholine (1 μM, 10 μM, 100 μM) was bath-applied for 2 min with a speed of about 2 ml/min, and followed by washout of 15 min. A neuron was excluded for data analysis if the change in series resistance was larger than 25 MΩ or 15% of baseline.

To verify whether CNO could silence hM4D-expressing RE neurons, AAV2/9-CaMKIIα-hM4d-mCherry virus (BrainVTA, China) were injected into the RE. After about 2 weeks of recovery, the coronal brain slices containing the RE were prepared. Action potentials in hM4D-expressing RE neurons were elicited by depolarizing the membrane potential in the current clamp configuration. After recording the baseline for about 5 min, CNO (Tocris, USA) was bath-applied for 2 min and then followed by washout.

In addition, to investigate whether CNO inhibited the activities of MEC neurons receiving RE hM4D-expressed inputs, similarly, AAV2/9-CaMKIIα-hM4d-mCherry virus (BrainVTA, China) were injected into the RE. MEC glutamatergic neurons were clamped in the depolarized state to evoke stable action potentials. Since the input of RE is mainly an excitatory, in order to prevent the influence of local inhibitory input to MEC neurons, the brain slices were continuously perfused in the ACSF with $GABA_A$ receptor blockers (Bicuculline, 10 μM). After recording the baseline for about 5 min, CNO was added for 2 min, and then followed by washout. And postsynaptic responses of MEC neurons were also recorded in the voltage-clamp mode to further explore whether the decrease in discharge is due to a decrease in excitatory inputs.

The on-line electrophysiological data were continuously recorded using an EPC10 recording system and the Patchmaster software v2x73 (HEKA). The electrical signals were processed with 4 kHz low-pass filter and digitalized at 10 kHz. The off-line data were analyzed by the Igor Pro 4.03 (WaveMatrics) or Mini Analysis Program 6.0 (Synaptosoft).

Histology

After completing all experiments, the mice were anesthetized and a lesion maker device (Ugo Basile, Italy) to deliver 0.5 mA direct current for 10 s to each of the electrode locations. Then, mice were perfused transcardially with ~20 ml 37 °C phosphate-buffered saline (PBS), followed by ~50 ml ice-cold 4% paraformaldehyde (PFA). The brain tissues were carefully extracted from the skull and postfixed in 4% PFA for 5 h, then transferred to 30% sucrose for dehydration at 4 °C overnight. Brains were coronally or sagittally sectioned at 40 μm using a freezing microtome (CM 3050S, Leica). Slices containing interested brain regions were washed three times (10 min each time) in PBS and then mounted on glass microscope slides, dried, and coverslipped with a DAPI-containing mounting media (F6057, Sigma, USA). The expression of fluorescent protein and location of electrode, optical fiber, cannula were identified. Only animals with accurate recording sites and good fluorescence expression will be included. Images were taken by fluorescence microscope (BX53, Olympus), digital slide scanner (SLIDEVIEW™ VS 200, Olympus), or confocal laser scanning microscopes (LSM 900, Zeiss).

Sleep-wake cycle analysis

All the experiments required EEG and EMG recording were performed by Cheetah 5.7.4 acquisition software (Neuralynx). EEG and EMG signals were amplified (Digital Lynx SX; Neuralynx, MO, USA) and band-passed filtered at 0.1–100 Hz and 100–1000 Hz, respectively. Off-line analysis of sleep-wakefulness stage was performed by the specialized software SleepSign 2.0 (Kissei Comtec). Wakefulness was characterized by desynchronized, low-amplitude EEG rhythms and elevated EMG activity with phasic bursts. NREM sleep was defined as synchronized, high amplitude and low frequency (0.5-4 Hz) EEG activity and lower EMG activity compared with wakefulness with no phasic bursts. REM sleep was defined as containing a pronounced theta rhythm with nearly no EMG activity[61].

Trajectory analysis

Behavioral tracking data were recorded via an overhead camera with Cheetah 5.7.4 acquisition software (Neuralynx) at a 30 Hz sample rate. Cheetah 5.7.4 produced automated tracking of the animal's position by the green LED light mounted on the headstage near the animal's head. Imaging and behavioral data were further processed to calculate the

distance in each trial. The distance values were obtained by the distance of two adjacent points ($x1$, $y1$) and ($x2$, $y2$). The number of errors entering the non-target arm was judged according to the video and manually counted.

Reactivation analysis

The analysis of reactivation intensity was calculated as previous studies[32,62]. Firing pattern of trials during the spatial learning behavior were extracted as a template, and firing pattern during post-training sleep was matched with the template to gain the reactivation strength. For both the template and match epochs, spike trains of MEC ensemble were divided into 100 ms bins and Z-transformed to get the matrices $Q_{template}^{trial}$ and $Q_{match}^{post-sleep}$. The correlation matrix $C_{template}$ ($N_{cells} \times N_{cells}$) of the template epoch was defined as follows:

$$C = \frac{1}{B} Q Q^T \tag{1}$$

In this formula, B is the total amount of time bins, Q is the $Q_{template}^{trial}$. PC analysis was applied to decompose the matrix $C_{template}$ into projectors $P^{(l)}$, which is associated to the eigenvalue λ_l.

$$C = \sum_l \lambda_l P^{(l)} \tag{2}$$

Further, to describe the similarities between the cell assemblies activated pattern of post-task sleep section and spatial learning experience, reactivation strength was calculated as follows:

$$R_l(t) = \sum_{i,j,i\neq j} Q'_{it} P_{ij}^{(l)} Q'_{jt} \tag{3}$$

In the given equation, Q' represents the Z-transformed spike trains during the post-task sleep section at time t. $R_l(t)$ quantifies the instantaneous correspondence between the ongoing activity and the lth coactivation template.

To obtain the significant PC signal in the template epoch, the root square of the eigenvalues of the correlation matrix $C_{template}$ of random datasets has been demonstrated to adhere to the Marcenko–Pastur distribution[63,64]. In the limit $B \to \infty$ and $N \to \infty$ with $q = B/N \geq 1$ fixed,

$$\rho(\lambda) = \frac{q}{2\pi\sigma^2} \frac{\sqrt{(\lambda_{max} - \lambda)(\lambda - \lambda_{min})}}{\lambda} \tag{4}$$

$$\lambda_{min}^{max} = \sigma^2 (1 \pm \sqrt{1/q})^2 \tag{5}$$

The σ^2 is the variance of the elements of the random matrix, and the Q matrix is Z-transformed. In the null hypothesis where Q template represents uncorrelated data, the correlations between spike trains are solely influenced by random fluctuations. Consequently, the eigenvalues of $C_{template}$ should fall within the range of λ_{max} and λ_{min}. Any eigenvalues exceeding λ_{max} indicate the presence of nonrandom correlations in the matrix, thus referred to as signal PC. On the other hand, components associated with eigenvalues between λ_{max} and λ_{min} are considered non-signal components. Trial-by-trial normalized z scores of the activation strength of the signal PC during the training epoch were plotted along the trace on the maze. Then the z scores were clustered based on the preferential position of PC-representing firing patterns.

Firing rate analysis

Electrophysiological data for single-unit spike sorting were processed using SpikeSort3D v2.5.2.0 (Neuralynx). Clustering of spikes and unit isolation procedures were in accordance with the previous study[61]. The raw data was resampled to 30 kHz and the power in the 600–6000 Hz range was computed. PC analysis was used to extract and represent the first two PC on a two-dimensional plot of detected spike events. Waveforms with similar PC were clustered by using K-means sorting method. The isolated cluster was considered as single unit recorded from the same neuron. Cross-channel artifacts were eliminated by cross-correlation histogram. Based on the previous study[5], the putative interneurons and putative glutamatergic neurons were distinguished according to their firing frequency and waveforms. The putative interneurons had high firing frequency and narrow width of spike waveforms, while the putative glutamatergic neurons had broad waves and low firing frequency. Firing rate histograms and rastergrams were created using the software NeuroExplorer 5.312 (Nex Technologies).

Local field potential analysis

For LFP analysis, power spectral density (PSD) was first extracted by the software NeuroExplorer 5.312 (Nex Technologies), which was further processed using the MATLAB 2021a. The PSD for each frequency band: delta: 0.5–4 Hz, theta: 4–12 Hz, low-frequency gamma: 25–48 Hz, and high-frequency gamma: 60–90 Hz. To analyze LFP changes in multiple frequency domains, the Morlet wavelet transform was calculated with the wavelet software package[65]. We plotted spectrograms of MEC LFP for both wakefulness and NREM sleep, and aligned them to timestamps of reactivation events during NREM sleep to observe characteristic LFP during relevant events. In the closed-loop optical inhibition experiment, we calculated spectral values for a 2-s time window around each marker by using NeuroExplorer Perievent Spectrograms features. These spectrogram data were then exported to MATLAB 2021a for further processing.

Isolated theta wave detection

To detect theta waves, we firstly downsampled the LFP to 200 Hz. Then we calculated both the frequency and the amplitude of the signals using a Morlet wavelet[65] and computed the amplitude of the theta wave (4–12 Hz) within a sliding window of 0.1 s using MATLAB 2021a. If the amplitude of one sliding window is larger than the mean plus one standard deviations of the whole period, then this window is classified as a theta event. For these theta events detected, we calculated the distribution of average time and theta power (%) that characterize theta events during post-training NREM sleep. Theta power (%) was calculated as the proportion value of LFP power (4–12 Hz) / LFP power (0.5–90 Hz).

Theta power-delta phase coupling analysis

To measure the strength of MEC theta-delta coupling during NREM sleep, delta phases were binned into π/20 intervals (−180° - +540°) and the mean power of theta waves (4–12 Hz) in each phase bin was calculated. The phase of the filtered LFP was computed using the Hilbert transform. To calculate the comodulogram between delta phase and theta power, bands of delta activity was band-pass filtered (centers at 0.5–4 Hz) with a zero-phase filter and phase-power coupling was measured for wavelet power between 4–12 Hz. To depict the strength of theta-delta coupling, MI was calculated as described previously[66,67]. The Kullback–Leibler (KL) distance, a variable which was widely used to measure how much the phase-power distribution deviates from a uniform distribution. The MI is obtained by dividing the KL distance by a constant factor [the logarithm of the number of phase bins], which takes the assume values of MI between 0 (no coupling) and 1 (perfect coupling). In case of data overfitting, raw LFP signals were randomly arranged and MI values were obtained for the shuffled group. Additionally, to further analyze the characteristic LFP during reactivation, the reactivation strength in each phase bin of delta wave and the theta power around reactivation peak were calculated.

LFP coherence and spike-theta phase-locking analysis

For LFP coherence analysis, native MEC and RE LFP signals first imported into the software NeuroExplorer 5.312 (Nex Technologies),

and then processed to get the LFP power spectrum using the wavelet transform code. With the coherence analysis method, LFP coherence was computed ranging multiple frequency bands (0.5–90 Hz) during both wakefulness and NREM sleep (number of tapers = 5, time-bandwidth product = 3). The reference channel recording general signals was set as the reference channel for recording the MEC signal.

For spike-theta phase-locking analysis, every spike of RE was assigned to its corresponding theta phase. Rayleigh's test for circular uniformity was applied to test the significance of phase-locking. The preferred phase and the locking strength were the argument and modulus, respectively, of the average vector of all spike events corresponding to the theta phase[5,68,69]. Inclusion in the analysis was exclusively limited to spikes of RE observed during NREM sleep.

Ca²⁺ signal and theta wave synchrony analysis

To analyze the correlation of RE Ca^{2+} signal and MEC LFP during NREM sleep, Ca^{2+} peaks of RE neurons projecting to MEC were manually marked. $\Delta F/F$ (%) was used to present the value of GCaMP7b fluorescence signals[70]. The normalized $\Delta F/F$ reflects the changes in the $\Delta F/F$ values relative to the baseline, which is defined as the period from −2 to −1 s before the peak of the Ca^{2+} signal. The theta ratio represents the proportion of theta power in relation to both theta and delta band power. The average value of the theta ratio during −2 to −1 s before the peak of the Ca^{2+} signal serves as a baseline, and any deviation from this baseline is calculated as Δtheta ratio.

Causality analysis

Causality analysis was conducted to analyze the temporal directionality of RE and MEC occurrences of theta events. LFP of RE and MEC were preprocessed with Morlet wavelet transform. Theta events of MEC was defined as the time series X, and theta events of RE was defined as the the time series Y. The significance level was set 0.05. The null hypothesis posits that the Y does not exert a Grangerian influence on X. Based on the Bayesian Information Criterion to choose the optimal lag length. F-statistic and critical value was calculated. We reject the null hypothesis if critical value is smaller than F-statistic.

Statistical analysis

The statistical analyses were conducted utilizing SigmaPlot 14.0 (Systat Software), GraphPad Prism 8.0 (GraphPad Software), SPSS Statistics 25.0 (International Business Machines Corporation) and MATLAB 2021a (Mathworks). Normality and equal variances were formally tested for each group of data. For data with normal distribution and equal variances, two-tailed paired or unpaired t tests, and analysis of variance (ANOVA) with post hoc test were performed for the comparisons between groups. Welch's t test was employed for normally distributed data with non-homogeneous variances. If data did not conform to the normal distribution, nonparametric tests were performed. Significant differences were accepted when $P < 0.05$.

Reporting summary

Further information on research design is available in the Nature Portfolio Reporting Summary linked to this article.

Data availability

All data generated in this study are provided within the article, Supplementary Information and Source Data file. Further information regarding to the findings in the present study are available from the corresponding authors upon request. Source data are provided with this paper.

Code availability

Custom made codes for reactivation, isolated theta wave detection, theta power-delta phase coupling analysis, spike-theta phase-locking analysis and mouse route tracking are available on GitHub (https://github.com/hechaochongqing/NC-RE-MEC-matlab-code-2024).

References

1. Buzsaki, G. The hippocampo-neocortical dialogue. *Cereb. Cortex* **6**, 81–92 (1996).
2. Buzsaki, G. & Moser, E. I. Memory, navigation and theta rhythm in the hippocampal-entorhinal system. *Nat. Neurosci.* **16**, 130–138 (2013).
3. Colgin, L. L. Rhythms of the hippocampal network. *Nat. Rev. Neurosci.* **17**, 239–249 (2016).
4. Liao, Y. et al. Spatial memory requires hypocretins to elevate medial entorhinal gamma oscillations. *Neuron* **112**, 155–173.e158 (2024).
5. Chen, Q. H. et al. Histamine enhances theta-coupled spiking and gamma oscillations in the medial entorhinal cortex consistent with successful spatial recognition. *Cereb. Cortex* **28**, 2439–2457 (2018).
6. Haam, J. & Yakel, J. L. Cholinergic modulation of the hippocampal region and memory function. *J. Neurochem* **142**, 111–121 (2017).
7. Gu, Z., Alexander, G. M., Dudek, S. M. & Yakel, J. L. Hippocampus and entorhinal cortex recruit cholinergic and NMDA receptors separately to generate hippocampal theta oscillations. *Cell Rep.* **21**, 3585–3595 (2017).
8. Teles-Grilo Ruivo, L. M. & Mellor, J. R. Cholinergic modulation of hippocampal network function. *Front. Synaptic Neurosci.* **5**, 2 (2013).
9. Chen, J. et al. Control of emotion and wakefulness by neurotensinergic neurons in the parabrachial nucleus. *Neurosci. Bull.* **39**, 589–601 (2023).
10. Born, J. & Wilhelm, I. System consolidation of memory during sleep. *Psychol. Res.* **76**, 192–203 (2012).
11. Staresina, B. P. et al. Hierarchical nesting of slow oscillations, spindles and ripples in the human hippocampus during sleep. *Nat. Neurosci.* **18**, 1679–1686 (2015).
12. Marshall, L., Cross, N., Binder, S. & Dang-Vu, T. T. Brain rhythms during sleep and memory consolidation: neurobiological insights. *Physiology* **35**, 4–15 (2020).
13. Ohno, M. Failures to reconsolidate memory in a mouse model of Alzheimer's disease. *Neurobiol. Learn Mem.* **92**, 455–459 (2009).
14. Mander, B. A. et al. Beta-amyloid disrupts human NREM slow waves and related hippocampus-dependent memory consolidation. *Nat. Neurosci.* **18**, 1051–1057 (2015).
15. Hao, Y. et al. Resveratrol and Sir2 reverse sleep and memory defects induced by amyloid precursor protein. *Neurosci. Bull.* **39**, 1117–1130 (2023).
16. Steriade, M. Cholinergic blockage of network- and intrinsically generated slow oscillations promotes waking and REM sleep activity patterns in thalamic and cortical neurons. *Prog. Brain Res.* **98**, 345–355 (1993).
17. Steriade, M., Nunez, A. & Amzica, F. Intracellular analysis of relations between the slow (<1 Hz) neocortical oscillation and other sleep rhythms of the electroencephalogram. *J. Neurosci.* **13**, 3266–3283 (1993).
18. Stroh, A. et al. Making waves: initiation and propagation of corticothalamic Ca^{2+} waves in vivo. *Neuron* **77**, 1136–1150 (2013).
19. Fiath, R. et al. Laminar analysis of the slow wave activity in the somatosensory cortex of anesthetized rats. *Eur. J. Neurosci.* **44**, 1935–1951 (2016).
20. Carpenter, F., Burgess, N. & Barry, C. Modulating medial septal cholinergic activity reduces medial entorhinal theta frequency without affecting speed or grid coding. *Sci. Rep.* **7**, 14573 (2017).
21. Loureiro, M. et al. The ventral midline thalamus (reuniens and rhomboid nuclei) contributes to the persistence of spatial memory in rats. *J. Neurosci.* **32**, 9947–9959 (2012).
22. Dolleman-van der Weel, M. J. et al. The nucleus reuniens of the thalamus sits at the nexus of a hippocampus and medial prefrontal cortex circuit enabling memory and behavior. *Learn Mem.* **26**, 191–205 (2019).

23. Angulo-Garcia, D. et al. Cell assemblies in the cortico-hippocampal-reuniens network during slow oscillations. *J. Neurosci.* **40**, 8343–8354 (2020).

24. Cholvin, T. et al. The ventral midline thalamus contributes to strategy shifting in a memory task requiring both prefrontal cortical and hippocampal functions. *J. Neurosci.* **33**, 8772–8783 (2013).

25. Hallock, H. L., Wang, A. & Griffin, A. L. Ventral midline thalamus is critical for hippocampal-prefrontal synchrony and spatial working memory. *J. Neurosci.* **36**, 8372–8389 (2016).

26. Ali, M. et al. Environmental enrichment enhances systems-level consolidation of a spatial memory after lesions of the ventral midline thalamus. *Neurobiol. Learn Mem.* **141**, 108–123 (2017).

27. Klein, M. M. et al. Ventral midline thalamus lesion prevents persistence of new (learning-triggered) hippocampal spines, delayed neocortical spinogenesis, and spatial memory durability. *Brain Struct. Funct.* **224**, 1659–1676 (2019).

28. Marshall, U. & Born, J. The contribution of sleep to hippocampus-dependent memory consolidation. *Trends Cogn. Sci.* **11**, 442–450 (2007).

29. Ego-Stengel, V. & Wilson, M. A. Disruption of ripple-associated hippocampal activity during rest impairs spatial learning in the rat. *Hippocampus* **20**, 1–10 (2010).

30. van de Ven, G. M., Trouche, S., McNamara, C. G., Allen, K. & Dupret, D. Hippocampal offline reactivation consolidates recently formed cell assembly patterns during sharp wave-ripples. *Neuron* **92**, 968–974 (2016).

31. Lu, Y. et al. A critical time-window for the selective induction of hippocampal memory consolidation by a brief episode of slow-wave sleep. *Neurosci. Bull.* **34**, 1091–1099 (2018).

32. Peyrache, A., Khamassi, M., Benchenane, K., Wiener, S. I. & Battaglia, F. P. Replay of rule-learning related neural patterns in the prefrontal cortex during sleep. *Nat. Neurosci.* **12**, 919–U143 (2009).

33. Tingley, D. & Peyrache, A. On the methods for reactivation and replay analysis. *Philos. T R Soc. B* **375**, 20190231 (2020).

34. Staresina, B. P., Niediek, J., Borger, V., Surges, R. & Mormann, F. How coupled slow oscillations, spindles and ripples coordinate neuronal processing and communication during human sleep. *Nat. Neurosci.* **26**, 1429–1437 (2023).

35. Helfrich, R. F., Mander, B. A., Jagust, W. J., Knight, R. T. & Walker, M. P. Old brains come uncoupled in sleep: slow wave-spindle synchrony, brain atrophy, and forgetting. *Neuron* **97**, 221–230 (2018).

36. Zimmerman, E. C. & Grace, A. A. Prefrontal cortex modulates firing pattern in the nucleus reuniens of the midline thalamus via distinct corticothalamic pathways. *Eur. J. Neurosci.* **48**, 3255–3272 (2018).

37. Ferraris, M. et al. The nucleus reuniens controls long-range hippocampo-prefrontal gamma synchronization during slow oscillations. *J. Neurosci.* **38**, 3026–3038 (2018).

38. Ferraris, M., Cassel, J. C., de Vasconcelos, A. P., Stephan, A. & Quilichini, P. P. The nucleus reuniens, a thalamic relay for cortico-hippocampal interaction in recent and remote memory consolidation. *Neurosci. Biobehav. R.* **125**, 339–354 (2021).

39. Lopez-Madrona, V. J. et al. Different theta frameworks coexist in the rat hippocampus and are coordinated during memory-guided and novelty tasks. *eLife* 9, e57313 (2020).

40. Heys, J. G., Schultheiss, N. W., Shay, C. F., Tsuno, Y. & Hasselmo, M. E. Effects of acetylcholine on neuronal properties in entorhinal cortex. *Front. Behav. Neurosci.* **6**, 32 (2012).

41. Palacios-Filardo, J. et al. Acetylcholine prioritises direct synaptic inputs from entorhinal cortex to CA1 by differential modulation of feedforward inhibitory circuits. *Nat. Commun.* **12**, 5475 (2021).

42. Cardin, J. A. et al. Driving fast-spiking cells induces gamma rhythm and controls sensory responses. *Nature* **459**, 663–U663 (2009).

43. Buzsáki, G. & Wang, X. J. Mechanisms of gamma oscillations. *Annu. Rev. Neurosci.* **35**, 203–225 (2012).

44. Brodt, S., Inostroza, M., Niethard, N. & Born, J. Sleep-A brain-state serving systems memory consolidation. *Neuron* **111**, 1050–1075 (2023).

45. Klinzing, J. G., Niethard, N. & Born, J. Mechanisms of systems memory consolidation during sleep. *Nat. Neurosci.* **22**, 1598–1610 (2019).

46. Maingret, N., Girardeau, G., Todorova, R., Goutierre, M. & Zugaro, M. Hippocampo-cortical coupling mediates memory consolidation during sleep. *Nat. Neurosci.* **19**, 959–964 (2016).

47. Latchoumane, C. F. V., Ngo, H. V. V., Born, J. & Shin, H. S. Thalamic spindles promote memory formation during sleep through triple phase-locking of cortical, thalamic, and hippocampal rhythms. *Neuron* **95**, 424–435 (2017).

48. Girardeau, G., Benchenane, K., Wiener, S. I., Buzsáki, G. & Zugaro, M. B. Selective suppression of hippocampal ripples impairs spatial memory. *Nat. Neurosci.* **12**, 1222–1223 (2009).

49. Vertes, R. P., Linley, S. B. & Hoover, W. B. Limbic circuitry of the midline thalamus. *Neurosci. Biobehav. Rev.* **54**, 89–107 (2015).

50. Griffin, A. L. The nucleus reuniens orchestrates prefrontal-hippocampal synchrony during spatial working memory. *Neurosci. Biobehav. Rev.* **128**, 415–420 (2021).

51. Maisson, D. J. N., Gemzik, Z. M. & Griffin, A. L. Optogenetic suppression of the nucleus reuniens selectively impairs encoding during spatial working memory. *Neurobiol. Learn Mem.* **155**, 78–85 (2018).

52. Hauer, B. E., Pagliardini, S. & Dickson, C. T. The reuniens nucleus of the thalamus has an essential role in coordinating slow-wave activity between neocortex and hippocampus. *eNeuro* **6**, ENEURO.0365-19.2019 (2019).

53. Mei, H., Logothetis, N. K. & Eschenko, O. The activity of thalamic nucleus reuniens is critical for memory retrieval, but not essential for the early phase of "off-line" consolidation. *Learn Mem.* **25**, 129–137 (2018).

54. Joo, H. R. & Frank, L. M. The hippocampal sharp wave-ripple in memory retrieval for immediate use and consolidation. *Nat. Rev. Neurosci.* **19**, 744–757 (2018).

55. Girardeau, G. & Lopes-dos-Santos, V. Brain neural patterns and the memory function of sleep. *Science* **374**, 560–564 (2021).

56. Fuchs, E. C. et al. Local and distant input controlling excitation in layer II of the medial entorhinal cortex. *Neuron* **89**, 194–208 (2016).

57. Trettel, S. G., Trimper, J. B., Hwaun, E., Fiete, I. R. & Colgin, L. L. Grid cell co-activity patterns during sleep reflect spatial overlap of grid fields during active behaviors. *Nat. Neurosci.* **22**, 609–617 (2019).

58. Cordon, I. et al. Theta-phase closed-loop stimulation induces motor paradoxical responses in the rat model of Parkinson disease. *Brain Stimul.* **11**, 231–238 (2018).

59. Li, Y. et al. Adenosine modulates the excitability of layer II stellate neurons in entorhinal cortex through A1 receptors. *Hippocampus* **21**, 265–280 (2011).

60. He, C. et al. Superficial layer-specific histaminergic modulation of medial entorhinal cortex required for spatial learning. *Cereb. Cortex* **26**, 1590–1608 (2016).

61. Ren, S. et al. The paraventricular thalamus is a critical thalamic area for wakefulness. *Science* **362**, 429–434 (2018).

62. Peyrache, A., Benchenane, K., Khamassi, M., Wiener, S. I. & Battaglia, F. P. Principal component analysis of ensemble recordings reveals cell assemblies at high temporal resolution. *J. Comput Neurosci.* **29**, 309–325 (2010).

63. Marčenko, V. A. & Pastur, L. A. Distribution of eigenvalues for some sets of random matrices. *Matematicheskii Sbornik* **1**, 457–483 (1967).

64. Sengupta, A. M. & Mitra, P. P. Distributions of singular values for some random matrices. *Phys. Rev.* **60**, 3389–3392 (1999).

65. Müller, R. et al. Automatic detection of highly organized theta oscillations in the murine EEG. *J. Vis. Exp.* **121**, 55089 (2017).

66. Tort, A. B. L. et al. Dynamic cross-frequency couplings of local field potential oscillations in rat striatum and hippocampus during performance of a T-maze task. *Proc. Natl. Acad. Sci. USA* **105**, 20517–20522 (2008).
67. Tort, A. B. L., Komorowski, R. W., Manns, J. R., Kopell, N. J. & Eichenbaum, H. Theta-gamma coupling increases during the learning of item-context associations. *Proc. Natl. Acad. Sci. USA* **106**, 20942–20947 (2009).
68. Tang, Q. S. et al. Pyramidal and stellate cell specificity of grid and border representations in layer 2 of medial entorhinal cortex. *Neuron* **84**, 1191–1197 (2014).
69. Tang, Q. S. et al. Anatomical organization and spatiotemporal firing patterns of layer 3 neurons in the rat medial entorhinal cortex. *J. Neurosci.* **35**, 12346–12354 (2015).
70. Yi, T. T. et al. A sleep-specific midbrain target for sevoflurane anesthesia. *Adv. Sci.* **10**, 2300189 (2023).

Author contributions

C.H., Z.A.H., J.H., S.C.R. and J.X.X. conceived the study. Z.A.H., C.H., F.L.L., J.X.X., and S.C.R. designed the experiments. Q.X., M.M.L., X.L.Z., J.H.G., X.L., R.Y.W., N.W., L.Q., Y.X.L., Z.H.Z., X.L. and C.H. executed the experiments and conducted statistical analysis. C.H., M.M.L., Q.X. and Z.A.H. wrote the paper with the help of C.G.J., F.G.Y. and J.H.. All authors read and commented on the manuscript.

Competing interests

The authors declare no competing interests.

Additional information

Supplementary information The online version contains supplementary material available at https://doi.org/10.1038/s41467-024-53522-9.

Correspondence and requests for materials should be addressed to Fenlan Luo, Zhian Hu or Chao He.

Peer review information *Nature Communications* thanks Xiao Yu and the other, anonymous, reviewer(s) for their contribution to the peer review of this work. A peer review file is available.

Reprints and permissions information is available at http://www.nature.com/reprints

Publisher's note Springer Nature remains neutral with regard to jurisdictional claims in published maps and institutional affiliations.